AGU PUBLICATIONS

JGR

Journal of Geophysical Research: Solid Earth

RESEARCH ARTICLE
10.1002/2015JB012313

Key Points:
- We infer the role of the Calabrian Arc in the northward propagation of tectonic stress
- An outlier detection scheme enabled the identification of nonrepresentative GPS stations
- An important portion of the Africa-Eurasia convergence is not transmitted through the Calabrian Arc

Correspondence to:
A. M. Marotta,
anna.maria.marotta@unimi.it

Citation:
Splendore, R., A. M. Marotta, and R. Barzaghi (2015), Tectonic deformation in the Tyrrhenian: A novel statistical approach to infer the role of the Calabrian Arc complex, *J. Geophys. Res. Solid Earth*, *120*, 7917–7936 doi:10.1002/2015JB012313.

Received 1 JUL 2015
Accepted 20 OCT 2015
Accepted article online 4 NOV 2015
Published online 27 NOV 2015

Tectonic deformation in the Tyrrhenian: A novel statistical approach to infer the role of the Calabrian Arc complex

Raffaele Splendore[1], Anna Maria Marotta[1], and Riccardo Barzaghi[2]

[1]Department of Earth Sciences "Ardito Desio", Università degli Studi di Milano, Milan, Italy, [2]Politecnico di Milano, DICA, Milan, Italy

Abstract A thermomechanical model is used to analyze the strain pattern due to the Africa-Eurasia convergence in the area that extends from the Calabrian Arc to the Alpine domain and the role that is played by the Calabrian Arc complex in controlling the northward propagation of the tectonic stress. After a preliminary analysis to eliminate GPS stations that are not representative of the main regional tectonic process, the predicted deformation is compared to that based on GPS observations by using a novel χ^2 test in which both data and model uncertainties are taken into account. A large amount of the tectonic force (at least 75%) that is associated with the Africa-Eurasia convergence is accommodated by the Calabrian Arc complex, which plays a crucial role in controlling the intraplate propagation of the stress in the south Tyrrhenian area. Furthermore, a strong lithosphere, which is characterized by a granite-type upper crust, diabase-type lower crust, and peridotite-type lithosphere mantle, must pave the south Tyrrhenian; and a soft lithosphere, which is characterized by a granite-type upper crust, granulite-type lower crust, and peridotite-type lithospheric mantle, must pave the surrounding area to reproduce the expected regional compression in the SE-NW direction and extension in the perpendicular direction. Finally, the local deformation at high latitudes is not sensitive to variations in the boundary conditions along a limited portion of the Calabrian Arc.

1. Introduction

The Central Mediterranean is a tectonically complex domain in which different regional and local processes, such as the slow convergence between the Africa and Eurasia plates [*DeMets et al.*, 1994]; the subduction of the Ionian oceanic lithosphere beneath the European lithosphere, particularly along the Apennines and the Calabrian Arc; trench retreat [*Faccenna et al.*, 2001; *Wortel and Spakman*, 2000; *Bassi et al.*, 1997]; oblique subduction [*D'Agostino and Selvaggi*, 2004]; and the independent behavior of different microplates [*D'Agostino and Selvaggi*, 2004; *D'Agostino et al.*, 2008; *Marotta and Sabadini*, 2008; *Palano et al.*, 2012], produce adjacent extensional and compressional tectonic domains [e.g., *Hollstein et al.*, 2003; *Montone et al.*, 2004; *Marotta and Sabadini*, 2008; *Serpelloni et al.*, 2010; *Splendore et al.*, 2010; *Palano*, 2015], such as back-arc basins and orogenic belts.

In the SE-NW Africa-Eurasia convergence, a main feature that characterizes the Calabrian Arc domain is the subduction of the Ionian lithosphere beneath the European lithosphere. Seismological analyses suggest that the Calabrian subduction is characterized by a narrow (<200 km) and steep (approximately 70°) NW-dipping Wadati-Benioff zone [e.g., *Selvaggi and Chiarabba*, 1995; *Koulakov et al.*, 2009]. In particular, tomographic images indicate a deep (>400 km), laterally discontinuous positive-velocity anomaly that is associated with the subducted slab and proceeds under the Apennines, the Calabrian Arc, and the Magrebide Chain [*Selvaggi and Chiarabba*, 1995; *Wortel and Spakman*, 2000; *Piromallo and Morelli*, 2003; *Koulakov et al.*, 2009; *Neri et al.*, 2009, 2012]. Tomography also indicates that the Calabrian and southern Apennine slabs are not directly linked [*Chiarabba et al.*, 2008] and that the subducted slab has already detached at the northern and southwestern portions of the Calabrian Arc [*Neri et al.*, 2009], which implies that the final detachment and the cessation of the subduction processes are geologically close.

The last 15 million years of the evolution of the Calabrian subduction have been characterized by the occurrence of the rollback of the Ionian lithosphere, which is associated with the opening of the Tyrrhenian back-arc basin [*Malinverno and Ryan*, 1986; *Faccenna et al.*, 2001]. The opening rates of the Tyrrhenian in the Neogene-Quaternary are estimated to be 50–70 mm/y, which is faster than contemporaneous plate

convergence, whereas present-day evidence suggests that the back-arc spreading has essentially stopped [*Faccenna et al*., 2001], as confirmed by GPS observations [*D'agostino and Selvaggi*, 2004] and tomographic image analysis [*Neri et al*., 2009].

GPS observations also indicate that the Calabrian Arc is still moving trenchward [*D'Agostino and Selvaggi*, 2004; *D'Agostino et al*., 2008, 2011], which implies an active shortening in the Ionian wedge that is caused by the gravitational flow of the whole Calabrian Arc under the effect of the difference in potential energy between its crest and the bottom of the Ionian Sea [*D'Agostino et al*., 2011]. Furthermore, the present-day velocity field and active deformation of the Calabrian Arc domain are mainly controlled by the recent fragmentation of the Adriatic promontory, which rigidly transferred Africa's motion to the orogenic belts during the Neogene into different microplates or blocks that behave independently and accommodate part of the Eurasia-Africa convergence [*D'Agostino et al*., 2008; *Marotta and Sabadini*, 2008].

The subduction of the Ionian and Adriatic lithosphere plays a secondary role in driving the deformation of the Calabrian Arc domain, although this process may still be locally active [*D'Agostino et al*., 2008]. Geological evidence confirms this hypothesis for both the Calabrian wedge [*Minelli and Faccenna*, 2010] and the Apulia escarpment [*Argnani*, 2009], which suggests that the Hyblean block is not rigidly connected to the Nubia plate. This scenario is supported by geodetic observations of distinct deformation belts that separate the Tyrrhenian, the Sicilian-Hyblean, and the Calabrian domains [*Palano et al*., 2012], although the interrelationships of the different blocks are not fully understood. This complex puzzle of blocks can affect the stress transmission in the Calabrian Arc domain, which lies in a key position for driving the geodynamics of the Central Mediterranean.

Previous numerical models suggest that a consistent part of the Africa-Eurasia convergence is absorbed either into the Calabrian subduction [*Marotta and Sabadini*, 2008] or through the whole Calabrian Arc zone [*Splendore et al*., 2010]. *Splendore et al*. [2010] suggested that only 50% of the convergence is transmitted to the European plate. Here we perform a novel statistical analysis to support the results of *Splendore et al*. [2010]. In particular, we compare the deformation field that is predicted by a finite element thermomechanical model and the observed deformation based on GPS velocity solutions by means of a χ^2 test that is performed at both short and long wavelengths in the area that extends from the Calabrian Complex to the Alpine border. Both the observed and predicted deformation are expressed in terms of the rate of elongation or shortening of the baselines that cross the study area (Figure 1), which is henceforth referred to as the *baseline rate*.

The present analysis is more reliable and novel than previous attempts to investigate how the forces that are associated with the Africa-Eurasia convergence are attenuated by the Calabrian arc complex [*Splendore et al*., 2010]. First, a comparative analysis is performed in terms of the baseline strain rates instead of velocities, which avoids possible biases from the differences between the reference frame in which the observed GPS velocities are obtained and the reference frame in which the model is set up. Second, the present comparative analysis accounts simultaneously for both observation and model uncertainties, the latter through the covariance function [*Barzaghi et al*., 2014; *Marotta et al*., 2015], and thus better constrains the statistical significance of the comparison.

2. Model Setup

We used the thermomechanical model that was described in *Splendore et al*. [2010] and used in *Barzaghi et al*. [2014] and *Marotta et al*. [2015] to analyze the role of the Calabrian Arc complex in transmitting the tectonic force due to the Africa-Eurasia convergence. This finite element model is based on a spherical thin sheet approach and calculates the horizontal velocity field of the study domain, starting from the Africa-Eurasia convergence velocity and the rheological stratification of the lithosphere (Figure 1). The details of the model's approach and the parameter values are summarized in Appendix A, Tables A1 and A2.

We consider three lithosphere stratifications among the 12 combinations in *Marotta et al*. [2015]: gra_gra_per, which accounts for granite (upper crust), granulite (lower crust), and peridotite (lithospheric mantle); gra_dia_per, which accounts for granite (upper crust), diabase (lower crust), and peridotite (lithospheric mantle); and qtz_dia_oli, which accounts for quartzite (upper crust), diabase (lower crust), and olivine (lithospheric mantle). These three rheological profiles are representative of an average soft (gra_gra_per) and hard (gra_dia_per

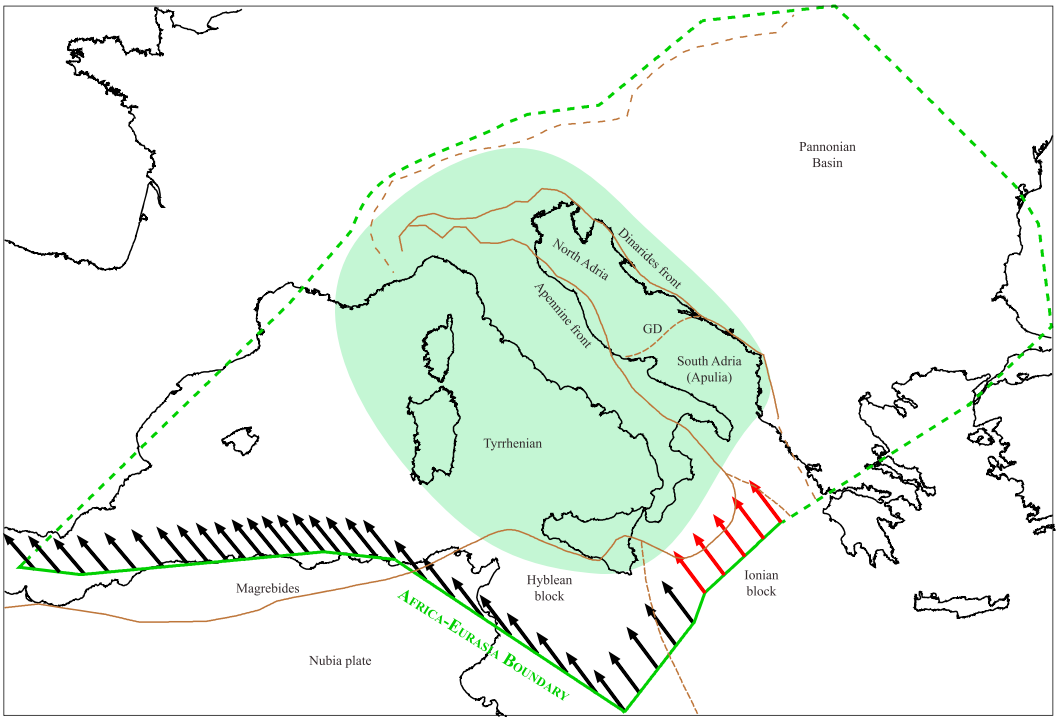

Figure 1. Sketch of the modeled domain. The green line represents the boundary of the finite element model mesh, and the arrows represent the Africa-Eurasia velocities, which were applied as boundary conditions on the southern boundary of the model. The red arrows represent the velocities, which vary from 0% to 100% of the Africa-Eurasia convergence rate, to analyze the Calabrian Arc complex absorption effect. The brown lines represent the principal plate boundaries in the modeled domain. GD stands for the Gargano-Dubrovnik fault zone. The study area is colored in green.

and qtz_dia_oli) lithosphere, respectively, and correspond to the best fit (gra_gra_per), an intermediate fit (gra_dia_per), and one of the worst fit models (qtz_dia_oli) in *Marotta et al.* [2015]'s statistical analysis. For each lithospheric stratification, we varied the Africa Eurasia convergence velocities in the proximity of the Calabrian Arc (Figure 1) at 0%, 25%, 50%, 75%, and 100% of the Africa-Eurasia relative velocity, which was calculated based on ITRF2005 [*Altamini et al.*, 2007] and following the procedure in *Nocquet et al.* [2001] (see *Splendore et al.*, 2010 for the detailed procedure). A total of 15 models were obtained (Appendix A; Tables A1 and A2).

In the following, we refer to each model as "lithosphere stratification.percentage of prescribed velocity" (e.g., gra_gra_per.25).

To statistically compare the model predictions to the GPS-derived observations, we applied the procedure that was described in *Barzaghi et al.* [2014] to each model and obtained a relative covariance matrix that was computed on the specific set of GPS permanent stations used in the present study (Table 1).

To retrieve the observed deformation field in the study area, we used the GPS velocity solutions of *Devoti et al.* [2011] for a set of 265 GPS stations that are distributed throughout the study domain (Table 1 and Figure 2).

3. Baseline Rate Computation

Starting from the velocity at each GPS station, baseline rates were computed from both the model predictions and GPS solutions along with the related uncertainties, as described in the following. Assuming a spherical Earth with radius R, the baseline rate $\dot{L}_{ij}$ between the two stations i and j can be expressed as

$$\dot{L}_{ij} = \frac{d}{dt}\left\{R \cdot \arccos\left[\sin\phi_i \sin\phi_j + \cos\phi_i \cos\phi_j \cos\left(\vartheta_i - \vartheta_j\right)\right]\right\},$$

Journal of Geophysical Research: Solid Earth

10.1002/2015JB012313

Table 1. List of the GPS-Derived Velocities With Their Corresponding Standard Deviations[a]

	ϑ	ϕ	V_ϑ	σ_{V_ϑ}	V_ϕ	σ_{V_ϕ}		ϑ	ϕ	V_ϑ	σ_{V_ϑ}	V_ϕ	σ_{V_ϕ}		ϑ	ϕ	V_ϑ	σ_{V_ϑ}	V_ϕ	σ_{V_ϕ}
Name	Long (deg)	Lat (deg)	(mm/yr)	(mm/yr)	(mm/yr)	(mm/yr)	Name	Long (deg)	Lat (deg)	(mm/yr)	(mm/yr)	(mm/yr)	(mm/yr)	Name	Long (deg)	Lat (deg)	(mm/yr)	(mm/yr)	(mm/yr)	(mm/yr)
ACOM	13.51	46.55	0.08	0.11	0.79	0.13	HFLK	11.39	47.31	0.55	0.25	0.76	0.33	PIPA	16.82	39.49	1.58	0.72	3.76	0.86
AFAL	12.17	46.53	−0.57	0.13	0.59	0.16	HMDC	14.78	36.96	−1.48	0.27	5.25	0.32	PLAC	16.44	38.45	0.78	0.47	3.81	0.53
AJAC	8.76	41.93	−0.68	0.19	0.62	0.23	IENG	7.64	45.02	0.33	0.14	−0.23	0.17	POFI	13.71	41.72	−0.94	0.67	2.05	0.82
ALES	8.62	44.92	−0.37	0.73	1.66	0.91	IGMI	11.21	43.80	0.49	0.53	2.55	0.66	PORA	10.11	45.89	0.51	0.96	0.83	1.25
AMPE	12.80	46.41	0.00	0.14	0.87	0.18	INGP	13.32	42.38	0.69	0.25	3.47	0.32	PORD	12.66	45.96	−0.49	0.26	1.21	0.34
AMUR	16.60	40.91	1.10	0.25	4.52	0.30	INGR	12.51	41.83	−0.78	0.24	2.20	0.29	PRAT	11.10	43.89	0.89	0.09	2.25	0.10
AQUI	13.35	42.37	0.83	0.14	2.83	0.17	IPRO	14.02	40.77	−2.04	0.39	1.02	0.48	PRMI	9.20	45.46	0.15	0.29	1.22	0.37
AQUN	13.38	42.34	0.13	1.06	2.50	1.35	ITFA	12.93	43.34	0.60	0.25	3.20	0.31	PSB1	14.81	41.22	0.28	0.45	3.12	0.55
AREZ	11.87	43.46	1.51	0.86	3.40	1.07	ITGT	12.78	43.23	1.17	0.35	2.60	0.42	PTRJ	14.53	41.36	0.74	0.46	2.59	0.57
ASCO	13.64	42.82	1.82	0.48	2.72	0.61	ITRA	14.00	42.66	1.20	0.47	2.93	0.58	PVIA	9.14	45.20	0.07	0.52	0.63	0.67
ASIA	11.53	45.87	−1.07	0.26	1.11	0.32	JOPP	15.89	38.61	1.57	0.36	3.27	0.42	PZIN	11.97	36.81	−0.48	0.55	1.82	0.62
ASTI	8.20	44.91	−0.11	0.67	0.59	0.85	KOET	13.01	46.67	−0.49	0.30	0.41	0.39	RAFF	14.36	37.22	−1.31	0.46	5.28	0.53
ATRA	14.01	42.55	0.93	0.59	2.91	0.73	LAMP	12.61	35.50	−2.93	0.08	3.84	0.10	REFO	12.70	42.96	0.49	0.25	1.94	0.30
BIEL	8.05	45.56	−0.21	0.34	−0.13	0.44	LARI	14.92	41.81	1.53	0.52	4.33	0.64	REMO	12.23	43.45	2.21	0.37	3.93	0.47
BOLG	11.36	44.50	0.02	0.51	3.98	0.66	LASP	9.84	44.07	0.36	0.25	0.75	0.31	RENO	13.09	42.79	0.95	0.25	2.23	0.30
BORM	10.36	46.47	−0.81	0.42	0.80	0.54	LAT1	12.90	41.47	−1.23	0.36	1.38	0.44	REPI	12.00	42.95	−0.26	0.33	1.94	0.41
BRAS	11.11	44.12	0.73	0.08	1.68	0.10	LEC1	9.41	45.86	−0.10	0.34	0.50	0.43	RETO	12.41	42.78	−0.39	0.25	1.63	0.31
BRBZ	11.94	46.80	0.29	0.57	0.74	0.77	LECC	9.41	45.86	−0.85	0.42	−0.07	0.53	RIET	12.86	42.41	0.21	0.93	0.18	1.16
BREA	10.23	45.56	−0.25	0.69	1.00	0.90	LI3D	15.11	38.64	−1.46	0.75	3.52	0.89	RMPO	12.70	41.81	0.20	1.25	1.28	1.48
BRIX	10.23	45.56	−0.02	0.21	0.43	0.27	LICO	14.05	40.88	−2.58	0.54	2.42	0.67	RNI2	14.15	41.70	1.63	0.41	3.11	0.49
BSSO	14.59	41.55	1.41	0.25	4.26	0.31	LNSS	13.04	42.60	0.81	0.36	2.21	0.44	ROVE	11.04	45.89	−0.32	0.55	1.14	0.67
BULG	15.38	40.08	0.41	0.36	3.31	0.43	LODI	9.47	45.29	0.45	0.40	1.05	0.52	ROVI	11.78	45.09	−0.33	0.33	2.05	0.42
BZRG	11.34	46.50	−0.76	0.14	0.70	0.18	LOSV	14.95	38.45	−1.00	0.78	6.41	0.91	RSMN	12.45	43.93	1.49	0.17	4.43	0.21
CADM	16.27	41.08	1.36	0.16	5.28	0.20	LUCC	10.50	43.85	0.47	0.45	1.46	0.57	RSPX	7.27	45.15	−0.01	0.37	−0.28	0.48
CAFE	15.24	41.03	−0.16	0.35	4.02	0.43	M0SE	12.49	41.89	−0.37	0.41	1.95	0.50	RSTO	14.00	42.66	1.38	0.10	3.43	0.11
CAGL	8.97	39.14	0.14	0.10	0.50	0.12	MABZ	10.55	46.69	0.43	0.41	1.40	0.54	SALO	10.52	45.62	0.54	0.52	−0.21	0.60
CAIE	12.25	43.47	0.24	0.44	2.06	0.56	MACE	13.45	43.29	2.53	0.51	3.72	0.63	SASA	17.96	40.39	1.90	0.69	4.29	0.81
CALA	11.16	43.87	1.28	0.38	1.73	0.48	MAGA	10.63	45.78	−1.06	0.29	0.22	0.37	SASS	8.57	40.72	0.06	0.65	0.28	0.81
CAME	13.12	43.11	1.92	0.11	3.59	0.13	MALT	14.53	35.84	−1.08	0.27	5.09	0.31	SAVI	7.66	44.65	0.60	0.59	−0.08	0.75
CAMO	16.45	39.34	1.90	0.59	3.74	0.77	MANT	10.79	45.16	−0.01	0.55	1.07	0.72	SBPO	10.92	45.05	−0.52	0.42	1.70	0.54
CANV	12.44	46.01	0.21	0.14	0.96	0.18	MAON	11.13	42.43	−0.45	0.24	0.99	0.30	SCHR	16.09	40.19	1.45	0.43	4.28	0.54
CARO	16.21	39.25	0.91	0.37	3.92	0.44	MARS	5.35	43.28	−0.08	0.17	−0.18	0.21	SCRA	14.00	42.27	0.32	0.58	3.40	0.73
CARP	10.43	45.37	0.21	0.42	0.18	0.54	MAT1	16.70	40.65	0.95	0.11	5.00	0.13	SCTE	18.47	40.07	0.92	0.45	4.42	0.53
CAVA	12.58	45.48	0.10	0.16	2.68	0.20	MATE	16.70	40.65	0.95	0.08	5.00	0.09	SERM	11.30	45.01	1.20	0.60	2.31	0.76
CCRI	16.78	39.23	1.94	0.48	4.27	0.53	MCEL	15.80	40.33	0.71	0.35	4.22	0.43	SERS	16.69	39.04	1.54	0.27	3.42	0.31
CDRU	15.30	40.49	−0.75	0.25	2.54	0.30	MCRV	15.17	40.78	1.94	0.36	3.92	0.43	SFEL	12.29	45.23	−0.63	0.28	1.49	0.36
CELL	15.89	38.26	1.25	0.61	2.47	0.68	MDEA	13.44	45.92	−0.41	0.13	2.52	0.16	SGIP	11.18	44.64	0.79	0.46	1.66	0.57
CERT	12.98	41.95	−1.21	0.45	2.08	0.56	MEDI	11.65	44.52	1.35	0.09	2.33	0.11	SGRT	15.74	41.75	1.83	0.44	5.63	0.54
CESI	12.90	43.01	0.44	0.55	3.79	0.65	MESA	15.55	38.18	0.78	0.55	2.59	0.64	SGTA	15.37	41.14	0.20	0.29	4.21	0.35
CETR	15.95	39.53	0.90	0.87	3.48	1.02	MESS	15.55	38.20	1.13	0.49	3.67	0.56	SIRI	15.87	40.18	0.94	0.37	4.67	0.44
CIGN	14.90	41.65	2.06	0.96	4.00	1.06	MILA	15.23	38.27	0.84	0.43	4.65	0.51	SLCN	15.63	40.39	−0.53	0.89	2.41	1.08
CITT	12.25	43.47	0.43	0.39	2.10	0.48	MILN	9.23	45.48	−0.25	0.49	0.90	0.63	SMRA	13.92	42.05	0.72	0.61	3.56	0.75
CMPR	15.30	40.32	−0.15	0.34	1.97	0.41	MILO	12.58	38.01	−1.08	0.15	3.32	0.17	SNAL	15.21	40.93	0.26	0.45	2.60	0.55
CODR	12.98	45.96	0.04	0.39	1.90	0.51	MMME	15.25	37.94	1.40	0.34	6.28	0.41	SPLT	16.44	43.51	0.55	0.78	3.24	0.97
COMO	9.10	45.80	0.11	0.16	−0.32	0.20	MOCA	11.14	46.10	−0.08	0.41	1.43	0.54	SSYX	15.08	37.16	−1.12	0.55	5.07	0.67
CORL	13.30	37.89	−1.72	0.26	4.13	0.31	MOCO	15.16	41.37	0.60	0.26	4.16	0.32	STBZ	11.43	46.90	0.36	0.35	0.98	0.45
COSE	16.31	39.20	0.58	0.28	2.91	0.34	MODA	6.71	45.21	−0.04	0.11	−0.05	0.14	STSV	16.92	39.15	3.04	0.34	3.42	0.40

AGU Journal of Geophysical Research: Solid Earth

10.1002/2015JB012313

Table 1. (continued)

	ϑ	ϕ	V_ϑ	σ_{V_ϑ}	V_ϕ	σ_{V_ϕ}		ϑ	ϕ	V_ϑ	σ_{V_ϑ}	V_ϕ	σ_{V_ϕ}		ϑ	ϕ	V_ϑ	σ_{V_ϑ}	V_ϕ	σ_{V_ϕ}
Name	Long (deg)	Lat (deg)	(mm/yr)	(mm/yr)	(mm/yr)	(mm/yr)	Name	Long (deg)	Lat (deg)	(mm/yr)	(mm/yr)	(mm/yr)	(mm/yr)	Name	Long (deg)	Lat (deg)	(mm/yr)	(mm/yr)	(mm/yr)	(mm/yr)
CPAN	15.08	38.64	1.52	0.63	3.12	0.71	MODE	10.95	44.63	−0.10	0.25	4.44	0.31	SVIN	15.23	38.80	−0.09	0.25	3.40	0.31
CRAC	16.44	40.38	1.55	0.35	4.69	0.43	MODR	13.88	41.15	−1.12	0.47	1.71	0.57	SVTO	16.44	40.60	0.05	0.50	4.87	0.60
CREA	9.69	45.35	0.14	0.32	0.65	0.42	MOGG	13.20	46.41	−0.22	0.14	1.46	0.18	TEOL	11.68	45.34	−0.21	0.20	2.60	0.26
CREM	10.00	45.15	0.30	0.32	1.51	0.41	MOIE	13.12	43.50	1.16	0.49	3.45	0.62	TGPO	12.23	45.00	0.47	0.63	1.81	0.80
CRLM	16.55	39.28	1.12	0.54	3.77	0.63	MONC	7.93	45.07	0.07	0.25	0.18	0.32	TGRC	15.65	38.11	0.63	0.18	3.91	0.22
CRMI	10.98	43.80	1.50	0.42	1.79	0.52	MOND	7.83	44.39	0.59	0.46	−0.23	0.57	TITO	15.72	40.60	0.31	0.25	5.11	0.29
CSSB	12.25	43.21	0.27	0.34	1.87	0.43	MOPS	10.95	44.63	1.63	0.63	3.63	0.80	TOLF	12.00	42.06	−1.54	0.25	1.87	0.31
CUCC	15.82	39.99	−0.19	0.22	3.75	0.27	MORB	9.57	46.13	−0.54	0.50	0.03	0.70	TORI	7.66	45.06	0.36	0.10	0.32	0.11
DALM	9.60	45.65	0.27	0.33	0.60	0.42	MOZZ	10.54	43.98	0.53	1.13	2.24	1.35	TRIE	13.76	45.71	−0.47	0.13	2.47	0.17
DARF	10.18	45.88	0.83	0.56	0.15	0.68	MPAZ	16.01	37.95	1.72	0.40	3.08	0.48	TRIV	14.55	41.77	1.62	0.52	4.23	0.63
DUBR	18.11	42.65	2.04	0.32	5.02	0.39	MPRA	12.99	46.24	−0.05	0.19	1.97	0.23	TVRN	16.23	39.43	0.96	0.39	4.15	0.47
ECNV	14.71	37.60	−1.17	0.40	3.79	0.46	MRLC	15.49	40.76	1.02	0.24	3.89	0.29	UDI1	13.25	46.04	−0.26	0.45	2.48	0.60
EIIV	15.08	37.51	1.20	0.20	2.22	0.23	MRRA	13.92	42.89	1.67	0.56	3.44	0.71	UDIN	13.25	46.04	−0.26	0.84	2.48	1.10
ELBA	10.21	42.75	−0.47	0.14	0.96	0.16	MRVN	16.20	41.06	0.79	0.35	4.40	0.43	UMBE	12.33	43.31	0.26	0.60	1.70	0.76
ENAV	14.33	40.58	−0.44	0.22	1.53	0.27	MSAG	15.91	41.71	1.10	0.37	3.87	0.46	UNFE	11.60	44.83	0.11	0.20	2.38	0.26
FASA	17.36	40.83	2.73	0.39	4.89	0.47	MSEL	11.65	44.52	1.24	0.25	2.61	0.32	UNOV	12.11	42.72	−0.26	0.55	1.38	0.68
FDOS	11.72	46.30	−0.38	0.39	0.90	0.53	MSRU	15.51	38.26	−0.72	0.18	5.30	0.22	UNPG	12.36	43.12	−0.27	0.27	1.83	0.34
FIGL	11.47	43.62	−0.04	0.68	2.05	0.86	MTRA	13.24	42.53	−0.92	0.60	0.83	0.73	UNTR	12.67	42.56	0.42	0.47	1.66	0.60
FRES	14.67	41.97	1.14	0.26	4.07	0.32	MTSN	15.75	40.27	1.02	0.83	4.07	0.99	UNUB	12.64	43.70	1.36	0.55	3.46	0.70
FROS	13.35	41.65	−0.28	1.11	2.48	1.36	MTTG	15.70	38.00	1.74	0.47	3.31	0.55	UPAD	11.88	45.41	0.22	0.24	1.49	0.32
FRRA	14.29	42.42	0.90	0.58	3.50	0.72	MTTO	12.99	42.46	0.77	0.51	1.49	0.64	UPG2	12.36	43.12	0.23	0.75	2.96	0.92
FRUL	14.23	40.88	0.33	0.91	2.69	1.10	MURB	12.52	43.26	0.81	0.21	2.03	0.27	USIX	13.18	38.71	0.12	0.27	2.44	0.32
GALF	14.57	37.71	−1.42	0.36	4.16	0.42	MVAL	12.41	43.38	0.94	0.39	2.49	0.49	VAGA	14.23	41.42	−0.84	0.19	2.49	0.22
GALG	8.31	40.56	0.15	0.34	0.65	0.41	NICE	7.30	43.73	0.61	0.15	0.73	0.19	VALC	12.28	43.28	0.25	0.50	2.24	0.62
GAVI	8.70	45.85	−0.13	0.66	−0.76	0.87	NOCI	17.06	40.79	2.13	0.35	4.41	0.42	VARZ	9.20	44.82	−0.08	0.53	0.98	0.69
GAZZ	9.83	45.79	0.69	0.44	−0.09	0.53	NOT1	14.99	36.88	−1.13	0.08	5.10	0.09	VCRA	13.50	42.74	1.77	0.69	3.19	0.87
GBLM	14.03	37.99	−0.85	0.33	5.57	0.41	NOTO	14.99	36.88	−1.13	1.15	5.10	1.36	VENE	12.33	45.44	0.22	0.18	2.21	0.24
GENO	8.92	44.42	0.22	0.10	0.23	0.12	NOVA	8.61	45.45	0.21	0.29	0.67	0.38	VENT	13.42	40.79	−0.62	0.60	2.05	0.75
GINA	5.79	43.68	0.08	0.10	0.21	0.11	ORID	20.79	41.13	0.51	0.13	−2.99	0.15	VERO	11.00	45.44	−0.18	1.09	1.11	1.41
GINO	16.76	40.58	2.09	0.42	4.86	0.50	PACA	14.56	40.87	−1.13	0.27	1.95	0.32	VIG3	8.86	45.31	0.37	0.48	0.44	0.62
GIOI	15.89	38.42	0.91	0.80	2.89	0.98	PADO	11.90	45.41	0.22	0.14	1.48	0.18	VIGE	8.86	45.31	1.30	0.46	0.00	0.60
GISI	9.10	39.75	−0.37	0.38	0.23	0.46	PALA	9.90	45.60	0.30	1.20	0.61	1.54	VITE	12.12	42.42	−1.63	1.05	1.69	1.32
GIUR	18.43	40.12	1.76	0.42	4.17	0.50	PALM	13.31	45.90	0.03	0.11	2.42	0.14	VLCH	13.85	46.61	0.86	0.11	1.27	0.13
GOLB	9.49	40.91	0.42	0.36	0.66	0.43	PALZ	15.96	40.94	0.95	0.39	4.80	0.47	VLKM	14.63	46.66	0.88	0.19	1.09	0.25
GRAS	6.92	43.75	0.26	0.09	0.23	0.10	PARM	10.31	44.76	0.92	0.25	2.40	0.31	VLSG	15.64	38.22	0.73	0.56	4.00	0.67
GRAV	7.02	45.13	0.43	0.53	−0.18	0.71	PATK	11.46	47.21	−0.26	0.11	1.50	0.15	VLUC	15.27	40.23	−0.36	0.20	2.30	0.25
GROG	9.89	43.43	0.15	0.25	0.79	0.32	PAVI	9.14	45.20	0.67	0.37	0.17	0.48	VOLT	11.91	45.38	−0.22	0.15	2.00	0.18
GROT	15.06	41.07	0.05	0.21	3.29	0.25	PBRA	14.23	42.12	0.74	0.57	4.33	0.67	VTRA	14.71	42.11	0.82	0.51	3.36	0.64
GSR1	14.54	46.05	0.17	0.23	2.41	0.30	PERU	12.39	43.11	0.45	0.63	2.17	0.76	VULT	15.62	40.95	1.05	0.63	4.54	0.76
GUAR	13.31	41.79	−0.15	0.46	1.09	0.57	PIAC	9.69	45.04	0.21	1.15	1.73	1.47	VVLO	13.62	41.87	0.14	0.25	2.60	0.31
HAGA	15.16	37.29	−1.24	0.37	5.13	0.44	PIET	12.40	43.45	0.34	0.46	2.58	0.58	ZOUF	12.97	46.56	−0.36	0.20	0.55	0.25
HAVL	15.12	36.96	−1.19	0.39	5.47	0.46														

[a]The solutions are taken from *Devoti et al.* [2011] and are calculated with respect to Eurasia Fixed.

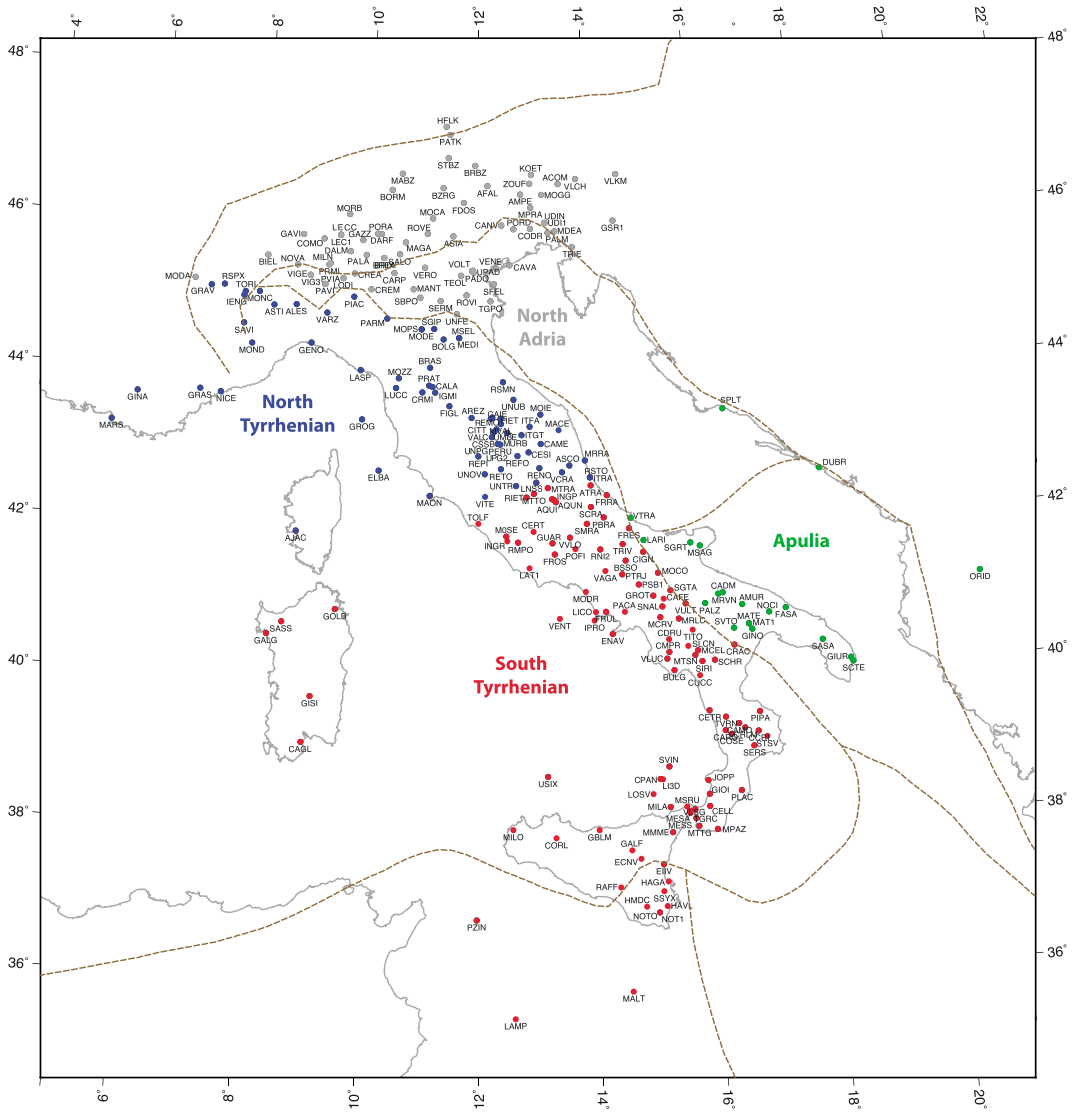

Figure 2. GPS stations (circles) that were used in the *Principal Component Analysis* (PCA). Different colors are used to distinguish the different subsets of the GPS stations that were used in the PCA analysis, which was performed at the local scale of the north Adria (gray), north Tyrrhenian (blue), south Tyrrhenian (red), and Apulia (green) subdomains. The brown lines indicate the principal plate boundaries from Figure 1.

where ϑ is the longitude and ϕ is the latitude or, after a few mathematical steps, $\dot{L}_{ij} = [\, B_{ji} \quad C_{ji} \quad B_{jj} \quad C_{jj} \,] \cdot \begin{bmatrix} V^i_\vartheta \\ V^i_\phi \\ V^j_\vartheta \\ V^j_\phi \end{bmatrix}$,

where

$$B_{ji} = \frac{\cos\phi_j \sin(\vartheta_i - \vartheta_j)}{d_{ij}}; \qquad C_{ji} = \frac{\sin\phi_i \cos\phi_j \cos(\vartheta_i - \vartheta_j) - \cos\phi_i \sin\phi_j}{d_{ij}};$$

$$B_{jj} = -\frac{\cos\phi_i \sin(\vartheta_i - \vartheta_j)}{d_{ij}}; \qquad C_{jj} = \frac{\cos\phi_i \sin\phi_j \cos(\vartheta_i - \vartheta_j) - \sin\phi_i \cos\phi_j}{d_{ij}};$$

$$d_{ij} = \sqrt{1 - \varepsilon_{ij}^2}; \qquad \varepsilon_{ij} = \sin\phi_i \sin\phi_j + \cos\phi_i \cos\phi_j \cos(\vartheta_i - \vartheta_j)$$

V^i_ϑ is the velocity component along the longitude, and $V_\phi{}^i$ is the velocity component along the latitude.

When N stations are considered simultaneously, the baseline rates along the $N_{\dot L} = \frac{N!}{(N-2)!2!}$ possible (nonrepeated) baselines can be calculated as

$$\begin{array}{cccccc}
\begin{matrix}\text{BASELINE}\\ \text{NUMBER}\end{matrix} & \begin{matrix}\text{STATION} & \text{STATION}\\ i=1,N-1 & j=i+1,N\end{matrix} & & \begin{matrix}\text{Baseline}\\ \text{Strain Rate}\end{matrix} & & \\
\left[\begin{array}{c} 1\\ 2\\ 3\\ \\ \\ \\ \\ \\ \\ \\ \\ \\ \\ \\ \\ \\ \cdot\\ \cdot\\ N_{\dot L}-1\\ N_{\dot L} \end{array}\right] &
\left[\begin{array}{cc}
 & 2\\
 & 3\\
 & 4\\
1 & \vdots\\
 & N-1\\
 & N\\ \hline
\vdots & \vdots\\ \hline
 & i+1\\
 & i+2\\
i & \vdots\\
 & N-1\\
 & N\\ \hline
\vdots & \vdots\\ \hline
 & N-1\\
N-2 & \\
 & N\\ \hline
N-1 & N
\end{array}\right] & \mapsto &
\left[\begin{array}{c} \dot L_{12}\\ \dot L_{13}\\ \dot L_{14}\\ \vdots\\ \dot L_{1\,N-1}\\ \dot L_{1N}\\ \vdots\\ \dot L_{i\,i+1}\\ \dot L_{i\,i+2}\\ \vdots\\ \dot L_{i\,N-1}\\ \dot L_{i\,N}\\ \vdots\\ \dot L_{N-2\,N-1}\\ \dot L_{N-2\,N}\\ \dot L_{N\,N} \end{array}\right] & = A\cdot &
\left[\begin{array}{c} V^1_\vartheta\\ V^1_\phi\\ V^2_\vartheta\\ V^2_\phi\\ \vdots\\ V^j_\vartheta\\ V^j_\phi\\ \vdots\\ V^{N-1}_\vartheta\\ V^{N-1}_\phi\\ V^N_\vartheta\\ V^N_\phi \end{array}\right],
\end{array}$$

where

$$A = \overset{\text{GPS station number}}{\left[\begin{array}{ccccccccccccccc}
\multicolumn{2}{c}{1} & \multicolumn{2}{c}{2} & \cdots & \multicolumn{2}{c}{i} & \cdots & \multicolumn{2}{c}{j} & \cdots & \multicolumn{2}{c}{N-1} & \multicolumn{2}{c}{N}\\
B_{21} & C_{21} & B_{22} & C_{22} & & & & & & & & & & & \\
 & & & & & & & & & & & & & & \\
 & & & & & B_{ji} & C_{ji} & & B_{jj} & C_{jj} & & & & & \\
 & & & & & & & & & & & & & & \\
 & & & & & & & & & & & B_{N\,N-1} & C_{N\,N-1} & B_{N\,N} & C_{N\,N}
\end{array}\right]}$$

Although the GPS velocities are assumed to be uncorrelated variables, the calculated baseline rates are not. The application of the classical rule of covariance matrix propagation allows the full covariance matrix that is associated with the baseline rates to be obtained as

$$C_{\dot L} = A \cdot C_v \cdot A^T,$$

where C_v is the $2N \times 2N$ symmetric matrix, whose diagonal terms contain the standard deviations σ^2_ϑ and σ^2_ϕ of the velocity components in Table 1.

When the above described procedure was adopted to calculate the observed and modeled deformation field, each GPS station was chosen as a reference site (now on *pole*), and the baseline rate was computed along all possible baselines that could be built with the remaining stations.

Furthermore, when the procedure was applied to calculate the modeled deformation field, the velocity solutions that were predicted by each model were interpolated onto the geodetic sites by the same shape function that was used for the numerical solution before computing the baseline rate along the same baselines that were used for the GPS data.

4. Geodetic Deformation Field

In the present section, we illustrate the main strain features that were observed in the study area (green area in Figure 1) in terms of the rate of elongation or shortening of baselines (baseline rate).

To calculate the observed baseline rates, we used the GPS velocity solutions that were recorded at the set of 265 GPS stations in Figure 2. Table 1 lists, for each GPS station, the longitude ϑ, the latitude ϕ, the absolute velocity components along the longitude V_ϑ along the latitude V_ϕ, and the corresponding velocity standard deviations $\sigma_{v\vartheta}$ and $\sigma_{v\phi}$.

The GPS-derived deformation field in the study domain has been described in recent publications, such as *Marotta and Sabadini* [2008]; *Barba et al*. [2010]; *Serpelloni et al*. [2010]; *Palano et al*. [2012], and *Palano* [2015], in terms of the geodetic strain rate. Generally, strong extension is described along the Apennine ridge, with a chain-perpendicular direction, and continuing along the Calabro-Peloritan ridge, whereas strong compression is observed in the southern part of the Tyrrhenian basin, with a N-S direction, and in the Gaeta Gulf, with an E-W direction. The Po Plain and the Adriatic region display compression that is perpendicular to the Apennine front. These observations agree with the measured borehole stresses [*Montone et al*., 2004] and seismological studies [*Presti et al*., 2013]. However, the described geodetic deformation pattern was computed after the interpolation of the observed velocities over a regular grid and reflects a small-scale strain rate field. By using the baseline rates, a larger-scale deformation can be computed without interpolating the GPS data. The baselines allow us to focus on the behavior of the system parallel and perpendicular to the main direction of the Africa-Eurasia convergence, which is roughly NW-SE, at long and short wavelengths by choosing a pair of distant or close GPS stations, respectively.

Figure 3 shows the geodetic deformation field at the regional scale in terms of the baseline rates that were computed starting from the whole GPS stations data set, which covers the entire study domain. When the baselines are calculated starting from the poles in the western part of the domain, such as AJAC and CAGL (Figures $3a_1$ and $3a_2$, respectively), strong, roughly E-W extension is observed, which reflects the relative eastward movement of the Apennines with respect to the Sardinia-Corsica block. The Africa-Eurasia convergence parallel baselines are characterized by shortening, with the strongest magnitude relative to the stations in the Hyblean block south of the plate boundary, which indicates active convergence west of the Calabrian Arc.

Choosing a pole in the northern portion of the domain, such as MONC (Figure $3b_1$), results in shortening in the direction of the Africa-Eurasia convergence, with the lowest rates along the Apennine chain parallel to the axis of the belt.

Strong shortening parallel to the Africa-Eurasia convergence direction is observed when a pole in the southern portion of the Tyrrhenian basin, such as MSRU, is chosen (Figure $3b_2$) and is associated with extension with respect to the poles in the Hyblean block. Finally, when poles roughly in the center of the study domain are chosen, such as MOIE and MRLC, (Figures $3c_1$ and $3c_2$, respectively), extension is observed perpendicular to the Africa-Eurasia convergence direction, which agrees with the eastward motion of the Apennine front. The shorter baselines that run perpendicular to the axis of the Apennine belt show extension, which agrees with previous studies [*Montone et al*., 2004; *Palano et al*., 2012; *Palano*, 2015], whereas compression parallel to the Africa-Eurasia convergence direction characterizes the NW-SE directed baselines.

To illustrate local deformation features, we performed an analysis of the deformation patterns by using the limited subsets of GPS stations, which are located within the north Tyrrhenian, south Tyrrhenian, north Adria, and Apulia subdomains and indicated by circles of different colors in Figure 2 (blue for the north Tyrrhenian, red for the south Tyrrhenian, gray for north Adria, and green for Apulia). The results are shown in Figure 4. Local features that contrast with the regional deformation pattern can be highlighted, which suggests the presence of local-scale processes that produce a second-order effect on short-scale deformation. When selecting STSV as the pole for the south Tyrrhenian or MODE as the pole for the north Tyrrhenian (Figure 4a), extension characterizes SE-NW baselines, which contrasts with the observed regional shortening

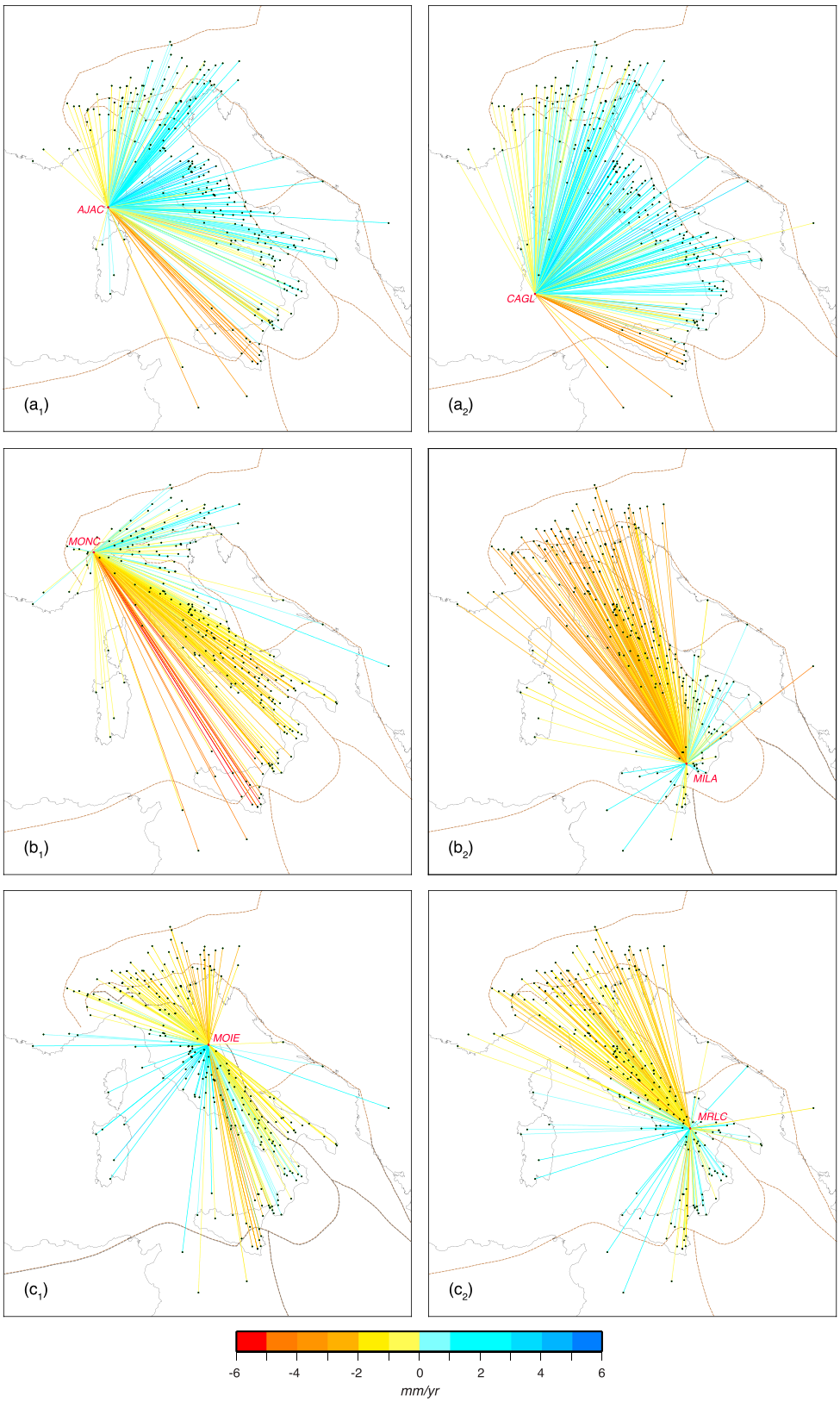

Figure 3. Regional scale deformation in terms of the baseline rates, which were computed starting from the GPS-derived velocities that cover the entire study area. Baselines were built for six sample poles throughout the study area: (a_1) AJAC, (a_2) CAGL, (b_1) MONK, (b_2) MILA, (c_1) MOIE, and (c_2) MRLC. The baselines are colored according to the associated strain rate (see the color scale for further details). The brown lines indicate the principal plate boundaries from Figure 1.

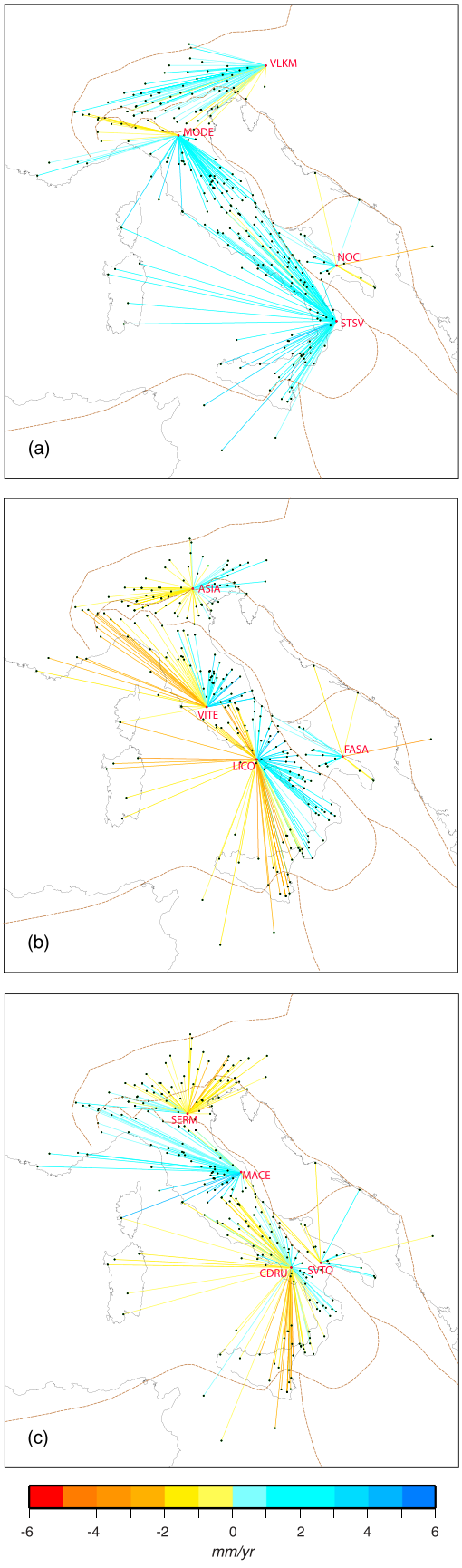

(Figure 3). Strong shortening along W-E baselines is observed when LICO and VITE are chosen as poles (Figure 4b), which is not compatible with the regional deformation pattern. When focusing on the north Adria domain, close poles, such as VLKM, ASIA, and SERM (Figures 4a–4c, respectively), show different behavior. A roughly similar behavior occurs within the south Adria domain (Apulia).

Because the Mediterranean is a complex tectonic area in which deformation is controlled by both regional and local geodynamic mechanisms, some of the available GPS stations may not be representative of the main regional process we are focusing on, that is, the Africa-Eurasia convergence and the related stress transmission through the Calabrian Arc complex. Thus, these stations may bias the interpretation of the results if included in the comparative analysis. We herein assume that the GPS velocity solutions that were recorded by these GPS stations are anomalies that can be treated as data outliers, that is, observations that are inconsistent with the remainder of the data. To increase the reliability of our analysis and its conclusions, we performed a preliminary analysis to identify outliers before performing the comparative analysis. Various statistical methods are available to detect outliers [*Markou and Singh*, 2003, and references therein]. Here we define a scheme that is based on Principal Component Analysis (PCA), as described in *Jolliffe* [2010].

Figure 4. Local scale deformation in terms of the baseline rates, which were computed starting from GPS-derived velocities. Each panel shows the baselines that were built for four sample poles, one for each subdomain: (a) VLKM, MODE, NOCI, and STSV; (b) ASIA, VITE, LICO, and FASA; (c) and SERM, MACE, CDRU, and SVTO. The baselines are colored according to the associated strain rate (see the color scale for further details). The brown lines indicate the principal plate boundaries from Figure 1.

5. PCA-Based Outlier Detection Analysis

We began by considering a GPS database that is composed of 265 (N) stations that are distributed throughout the study area (Table 1 and Figure 2). Figure 5a$_1$ presents a plot of the data (red-filled squares) in terms of the velocity components along the longitude, V^i_ϑ, and along the latitude, V^i_ϕ.

The corresponding average values, $\overline{V}_\vartheta$ and $\overline{V}_\phi$, are subtracted from each component of the GPS horizontal velocities to obtain a new data set whose mean is zero (black empty squares in Figure 5a$_1$, coincident with the red-filled squares), which enables the construction of a $N \times 2$ matrix, X, called the *Mean Adjusted Data*:

$$\text{Mean Adjusted Data X} = \begin{bmatrix} \Delta V^1_\vartheta & \Delta V^1_\phi \\ \Delta V^2_\vartheta & \Delta V^2_\phi \\ \cdots & \cdots \\ \Delta V^N_\vartheta & \Delta V^N_\phi \end{bmatrix} = \begin{bmatrix} \left(V^1_\vartheta - \overline{V}_\vartheta\right) & \left(V^1_\phi - \overline{V}_\phi\right) \\ \left(V^2_\vartheta - \overline{V}_\vartheta\right) & \left(V^2_\phi - \overline{V}_\phi\right) \\ \cdots & \cdots \\ \left(V^N_\vartheta - \overline{V}_\vartheta\right) & \left(V^N_\phi - \overline{V}_\phi\right) \end{bmatrix}.$$

By using the Mean Adjusted Data Matrix X, the *Covariance Matrix* C_{ss} is then computed as follows:

$$C_{ss} = \begin{bmatrix} C_{ss}^{\vartheta\vartheta} & C_{ss}^{\vartheta\phi} \\ C_{ss}^{\vartheta\phi} & C_{ss}^{\phi\phi} \end{bmatrix} = \frac{1}{N-1} \cdot X^T \cdot X = \frac{1}{N-1} \cdot \begin{bmatrix} \sum_{i=1}^{N} \left(\Delta V^i_\vartheta\right)^2 & \sum_{i=1}^{N} \left(\Delta V^i_\vartheta \cdot \Delta V^i_\phi\right) \\ \sum_{i=1}^{N} \left(\Delta V^i_\vartheta \cdot \Delta V^i_\phi\right) & \sum_{i=1}^{N} \left(\Delta V^i_\phi\right)^2 \end{bmatrix}.$$

As part of the standard PCA procedure, the eigenvalues $\begin{bmatrix} eig_1 & eig_2 \end{bmatrix}$ and eigendirections $\begin{bmatrix} \hat{n}_1 & \hat{n}_2 \end{bmatrix}$ of C_{ss} are then computed.

Once the eigenvectors are plotted on top of the Mean Adjusted Data (dashed black lines in Figure 5a$_1$), the first eigenvector, which is associated with the highest eigenvalue, defines the principal pattern of the data, which may be attributable to the direction of the principal tectonic process that controls the distribution of the recorded velocity field; we herein refer to this eigenvector as the *Principal Direction*:

$$\text{Principal Direction} : \hat{n}_1 = \begin{bmatrix} \hat{n}_{\vartheta_1} & \hat{n}_{\phi_1} \end{bmatrix}.$$

The second and smaller eigenvector defines the less important patterns of the data and might be related to other local tectonic processes that, along with Africa-Eurasia convergence, define the observed regional deformation pattern.

We obtain the *Projected Data* (black-filled circles in Figure 5a$_1$) by ignoring the eigenvector that is related to the smaller eigenvalue and by projecting the Mean Adjusted Data along the Principal Direction:

$$\begin{aligned} \text{Projected Data} &= \begin{bmatrix} \overset{\text{projec}}{\Delta V^1} & \overset{\text{projec}}{\Delta V^2} & \ldots & \overset{\text{projec}}{\Delta V^N} \end{bmatrix} \\ &= \begin{bmatrix} \hat{n}_{\vartheta_1} & \hat{n}_{\phi_1} \end{bmatrix} \cdot \begin{bmatrix} \left(V^1_\vartheta - \overline{V}_\vartheta\right) & \left(V^2_\vartheta - \overline{V}_\vartheta\right) & \ldots & \left(V^N_\vartheta - \overline{V}_\vartheta\right) \\ \left(V^1_\phi - \overline{V}_\phi\right) & \left(V^2_\phi - \overline{V}_\phi\right) & \ldots & \left(V^N_\phi - \overline{V}_\phi\right) \end{bmatrix} \end{aligned}$$

After multiplying the Projected Data by the transposed *Principal Direction* and summing the average values, $\overline{V}_\vartheta$ and $\overline{V}_\phi$, we can obtain the Adjusted Data, which can be compared to the original GPS velocities:

$$\text{Adjusted Data} = \begin{bmatrix} \overset{\text{adjusted}}{V^1_\vartheta} & \overset{\text{adjusted}}{V^2_\vartheta} & \cdots & \overset{\text{adjusted}}{V^N_\vartheta} \\ \overset{\text{adjusted}}{V^1_\phi} & \overset{\text{adjusted}}{V^1_\phi} & \cdots & \overset{\text{adjusted}}{V^N_\phi} \end{bmatrix} = \begin{bmatrix} \overline{V}_\vartheta \\ \overline{V}_\phi \end{bmatrix} + \begin{bmatrix} \hat{n}_{\vartheta_1} \\ \hat{n}_{\phi_1} \end{bmatrix} \cdot \begin{bmatrix} \overset{\text{projec}}{\Delta V^1} & \overset{\text{projec}}{\Delta V^2} & \cdots & \overset{\text{projec}}{\Delta V^N} \end{bmatrix}.$$

We performed a standard statistical analysis over the residual velocities, that is, the differences between the original GPS velocities and the estimated PCA velocities, to identify the GPS stations at which the recorded velocities are inconsistent with the dominant tectonic mechanism that is associated with the Africa-Eurasia convergence. The standard deviation of the residual velocities was computed for each component. GPS stations at which both component residual velocities were higher than 2 times the related standard deviations (green band in Figure 5a) were considered outliers.

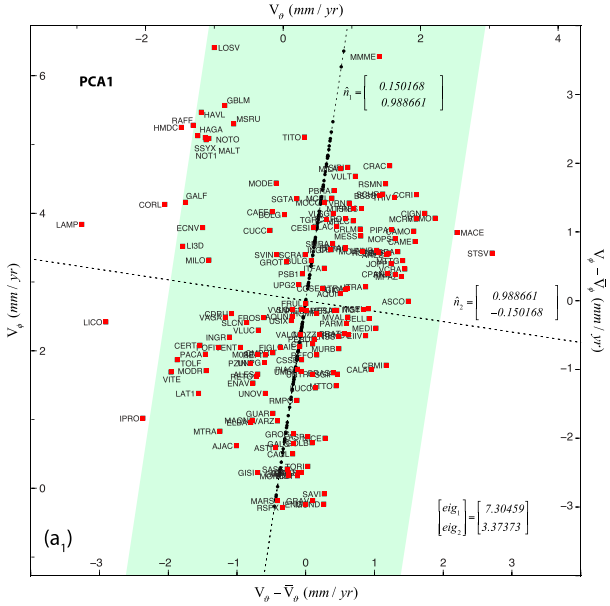

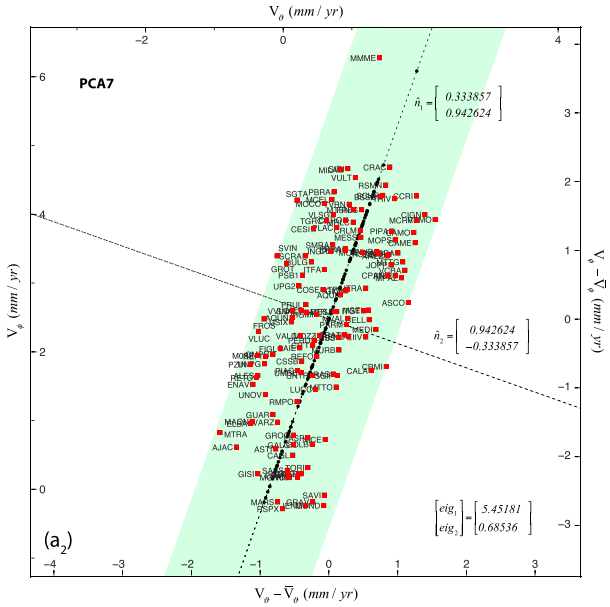

(a3)

Domain	Italy	Tyrrhenian	Apulia	Northern Adria
Number of used GPS stations	265	175	20	70
Number of excluded GPS stations	48 (18%)	38 (22%)	2 (10%)	14 (20%)
Number of PCA iterations	6	7	2	5
Principal Direction $\hat{n}_1$	[0.335525;0.942031]	[0.333857;0.942624]	[0.143083;0.989711]	[-0.134197; 0.990955]
Standard deviation σ_x	0.465708	0.477874	0.472619	0.286629
Standard deviation σ_ε	0.165873	0.169253	0.068325	0.038816

Figure 5. (a_1 and a_2) Results of the PCA analysis with the GPS-velocity database that covers the entire study area (Italy data set). The red-filled squares represent the plot of the data in terms of the velocity components along the longitude, V^i_ϑ, and along the latitude, V^i_ϕ. The black empty squares represent the data after subtracting the average value for each component (coincident with the red-filled squares). The black dashed lines correspond to the *eigendirections*. The black-filled circles represent the Projected Data. The green band represents the 2σ interval after the first PCA iteration, Figure 5a_1, and after the last iteration, Figure 5a_2. Stations that were located outside the green band were excluded after each iteration. Panel a_3 summarizes the results of the PCA analysis with the entire Italy dataset and with the different local datasets, which are shown with different colors in Figure 2.

We iteratively repeated the PCA and the successive statistical procedures and stopped at the seventh iteration, when no outliers were identified based on the applied 2σ criterion (Figure 5a$_2$).

Thus, after seven iterations, we identified a total of 48 GPS stations as outliers, which are listed in Figure 6a along with their areal distribution. The velocities that were recorded by these stations and the related baseline rates were excluded from the successive χ^2 analysis.

An identical PCA procedure was performed for the Tyrrhenian, the north Adria and the Apulia domains. Figure 5a$_3$ summarizes the results. Figure 6 shows the outliers for the Tyrrhenian (b), north Adria (c), and Apulia (d) subdomains.

6. χ^2 Comparative Analyses

We compared the baseline rates that were predicted by the 15 models to the baseline rates that were derived from the GPS velocity solutions by means of a χ^2 test. In the statistical test, we took into account both model and data uncertainties, following the procedure that was described in *Barzaghi et al*. [2014] and *Marotta et al*. [2015] after adapting it to the baseline rates:

$$\chi^2 = R^T \left(C_L^{\mathrm{GPS}} + C_L^{\mathrm{model}} \right)^{-1} R,$$

where R is the difference between the GPS velocity-derived baseline rates and the geophysical model's predicted baseline rates, C_L^{GPS} is the covariance matrix that is associated with the GPS velocity-derived baseline rates and C_L^{model} represents the covariance matrix that is associated with the geophysical model's baseline rates.

The comparative analysis was performed at the regional and local scales.

The χ^2 test was performed for each pole separately, and the results were then averaged over all poles for each model.

Figure 7a shows the results of the χ^2 test for the entire study domain. All the models, independently from the rheological stratification, show a clear increase in their agreement with the decrease in the percentage of transmitted AF-EU convergence, with a maximum variation of approximately 15 in the χ^2 values for the gra_gra_per model.

The gra_gra_per model was the worst at reproducing the regional deformation pattern for all the boundary conditions configurations. This rheological stratification, which is somewhat softer than gra_dia_per and qtz_dia_oli, exhibited minimal χ^2 values for 0% of the transmitted Africa-Eurasia convergence. The rheologically harder models (gra_dia_per and qtz_dia_oli) exhibited comparable χ^2 values, with a minimum corresponding to 0–25% of the transmitted Africa-Eurasia convergence.

The behavior of the models in response to the changes in boundary conditions, i.e., the variation in the transmitted convergence, suggests that an important portion of the Africa-Eurasia convergence is not transmitted through the Calabrian Arc, in which the subduction or accommodation of the rigid micro-blocks absorbs part of the push force because of the plate collisions, as already suggested by previous statistical analyses [*Splendore et al*., 2010; *Marotta et al*., 2015].

To verify the stability of this major result, we performed the χ^2 analysis within the Tyrrhenian, north Adria, and Apulia subdomains, (Figures 7b, 7e, and 7f, respectively). When the χ^2 analysis was limited west of the Apennine Front (Figure 7b), the general χ^2 trend did not change, with a slight increase in the agreement between the models and data, and the minimum χ^2 value occurs for the gra_dia_per model at 25% of the transmitted Africa-Eurasia convergence.

When the χ^2 analysis was performed at the smaller scale of the south and north Tyrrhenian, the results showed that in the north Tyrrhenian the χ^2 values did not vary, either for large variations in the percentage of the transmitted Africa-Eurasia convergence (Figure 7d), while a χ^2 trend similar to that obtained in the entire Tyrrhenian was predicted in the south Tyrrhenian, with even lower values of χ^2 (Figure 7c) in the north Tyrrhenian, which indicates that deformation at long distances is not affected by variations in the boundary conditions along the Calabrian Arc complex. Furthermore, a softer lithosphere (gra_gra_per stratification) in this subdomain better reproduces the local deformation pattern. These results were confirmed by the χ^2 analysis in the north Adria subdomain (Figure 7e), where models showed much less sensitivity to changes in boundary conditions. Thus, only distinguishing a best fit *lithosphere stratification* (gra_gra_per) in both the north Tyrrhenian and north Adria domains, rather than a best fit model, is possible.

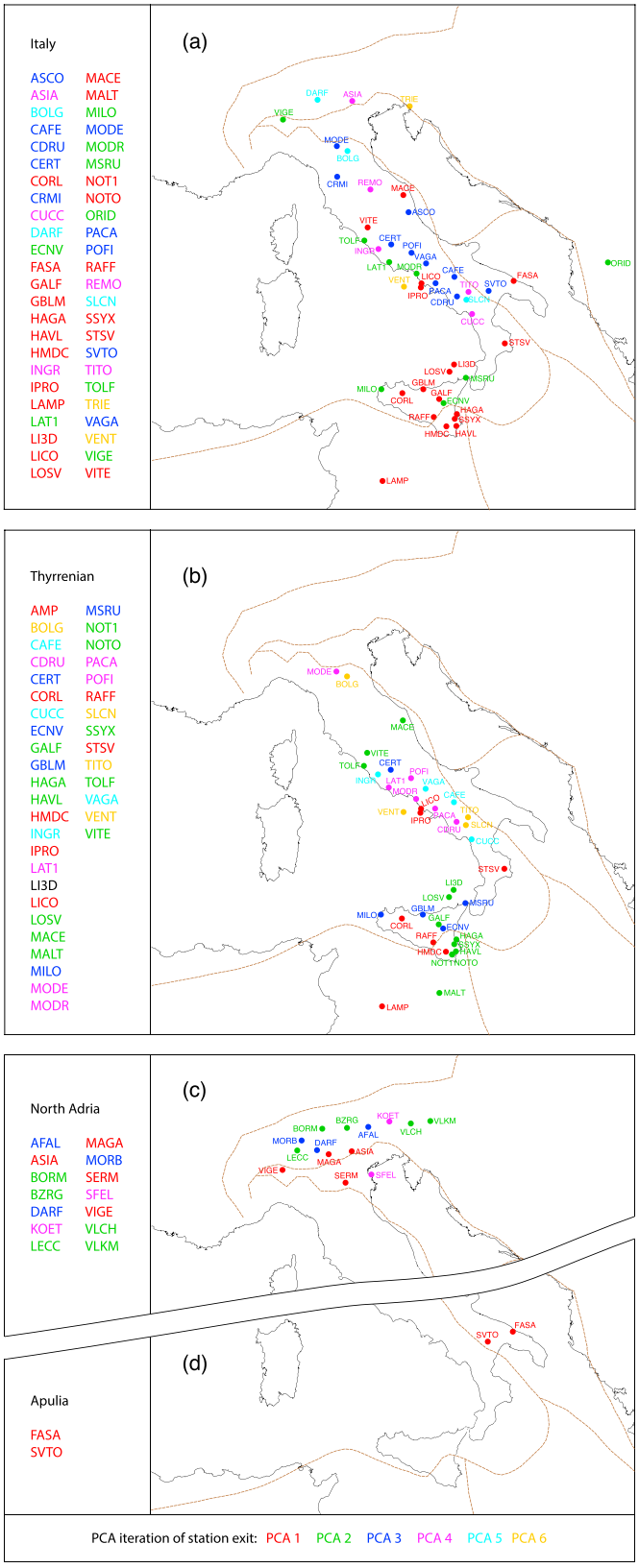

Figure 6. Lists of the GPS stations that were excluded after the PCA analysis from the (a) entire Italy data set and from the (b) Tyrrhenian, (c) north Adria, and (d) Apulia subsets. Different colors indicate the different PCA iterations for each station. The brown lines indicate the principal plate boundaries from Figure 1.

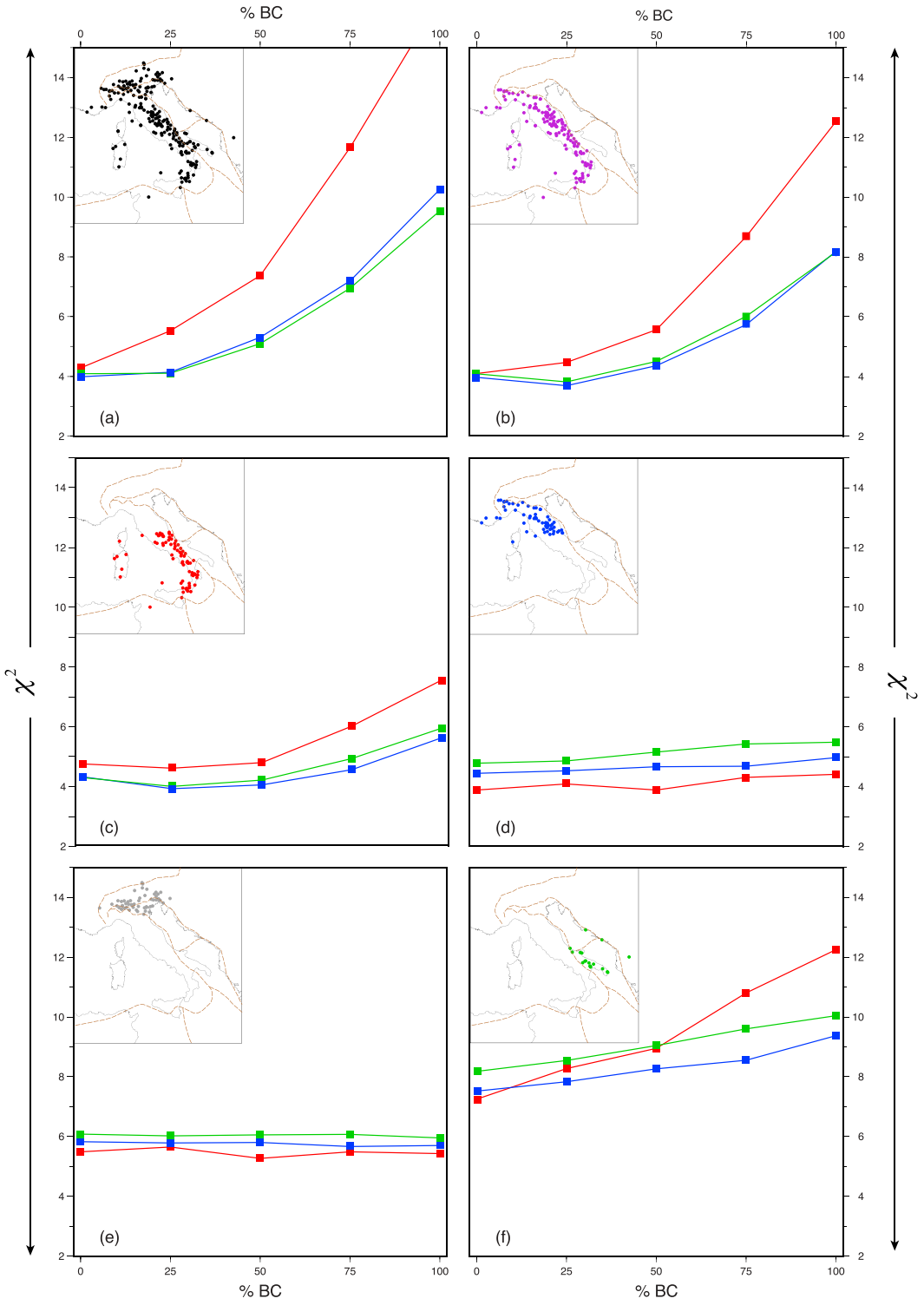

Figure 7. Results of the χ^2 test that was performed for the baseline rates at both the (a) regional scale of the entire study area and the local scale of the (b) Tyrrhenian; (c) south Tyrrhenian, (d) north Tyrrhenian, (e) north Adria, (f) and Apulia. The χ^2 values are averaged over the poles and are represented as a function of the % of transmitted convergence. The red lines and squares correspond to the gra_gra_per models, the blue lines and squares correspond to the gra_dia_per models, and the green lines and squares correspond to the qtz_dia_oli models. The colored circles in the insets of each panel indicate the GPS stations that were used in the χ^2 analysis.

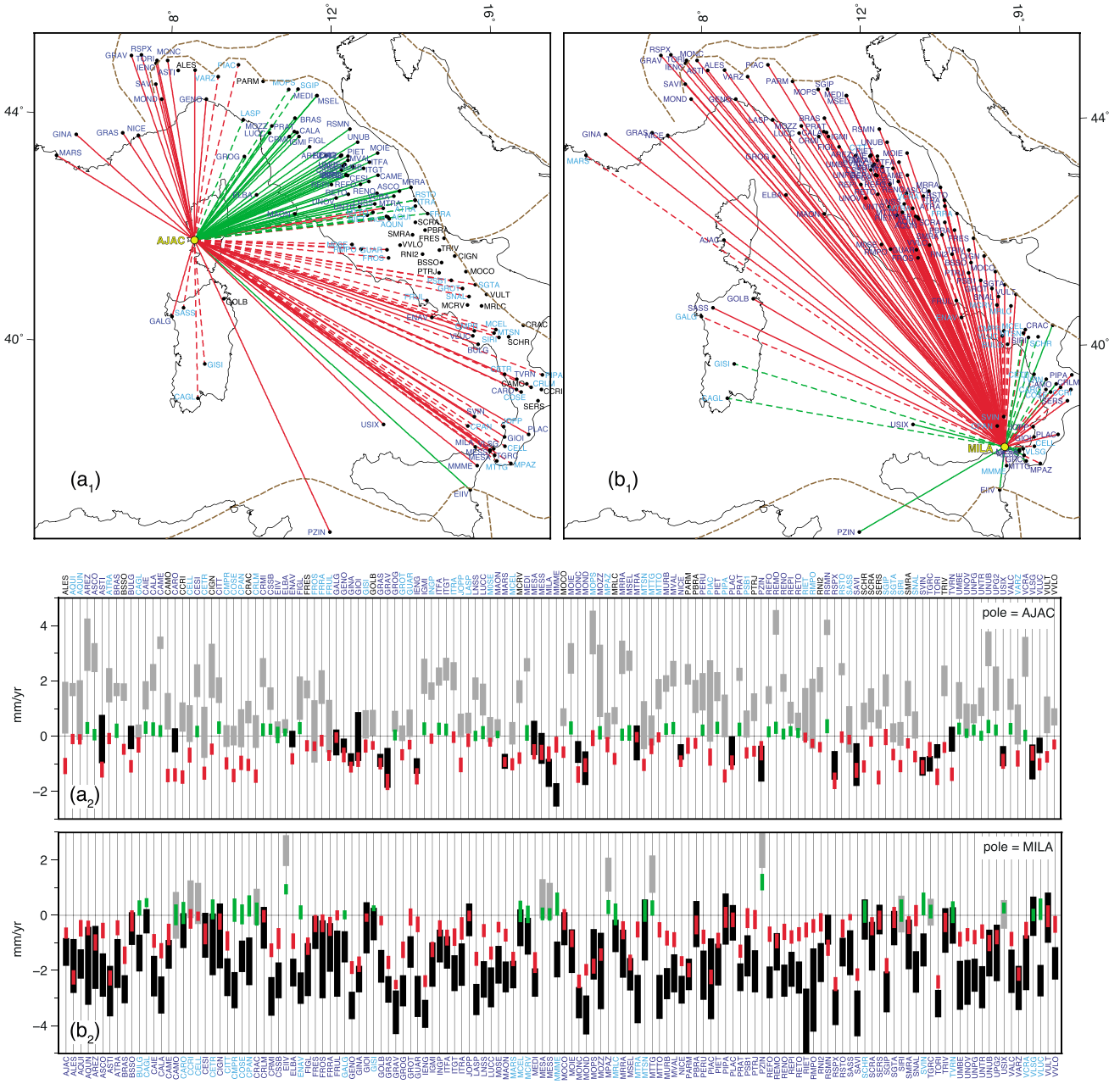

Figure 8. Large-scale strain pattern that is predicted along the baselines that cross the Tyrrhenian domain with respect to (a_1) AJAC and (b_1) MILA for the best fit model gra_dia_per.25 (red lines indicate shortening; green lines indicate elongation). Continuum lines are used when a good agreement between the predicted and geodetic strain rate is obtained. Dashed lines are used when the predicted and geodetic strain rates exhibit opposite trends but reconcile within their uncertainties. In Figures 8a_2 and 8b_2, the predicted (red for shortening and green for elongation) and geodetic (filled black rectangles for shortening and gray rectangles for elongation) baseline rate values are compared with their uncertainties for poles (a_2) AJAC and (b_2) MILA. The text is colored in blue when the predicted and geodetic baseline rate values agree, light blue is used when the predicted and geodetic baseline rate values reconcile within their uncertainties, and black is used when the agreement is poor.

The comparison between the χ^2 values at the regional scale of the entire study area and the Tyrrhenian to those that were obtained at the scale of the subdomains suggests that accounting for long baselines that connecting GPS stations near the Calabrian Arc complex to GPS stations at high latitudes, where the deformation is not sensitive to variations in the boundary conditions along the limited border of the Calabrian Arc, worsened the agreement between the data and the model, especially for high percentages of transmitted Africa-Eurasia convergence (compare Figure 7c to Figures 7a and 7b).

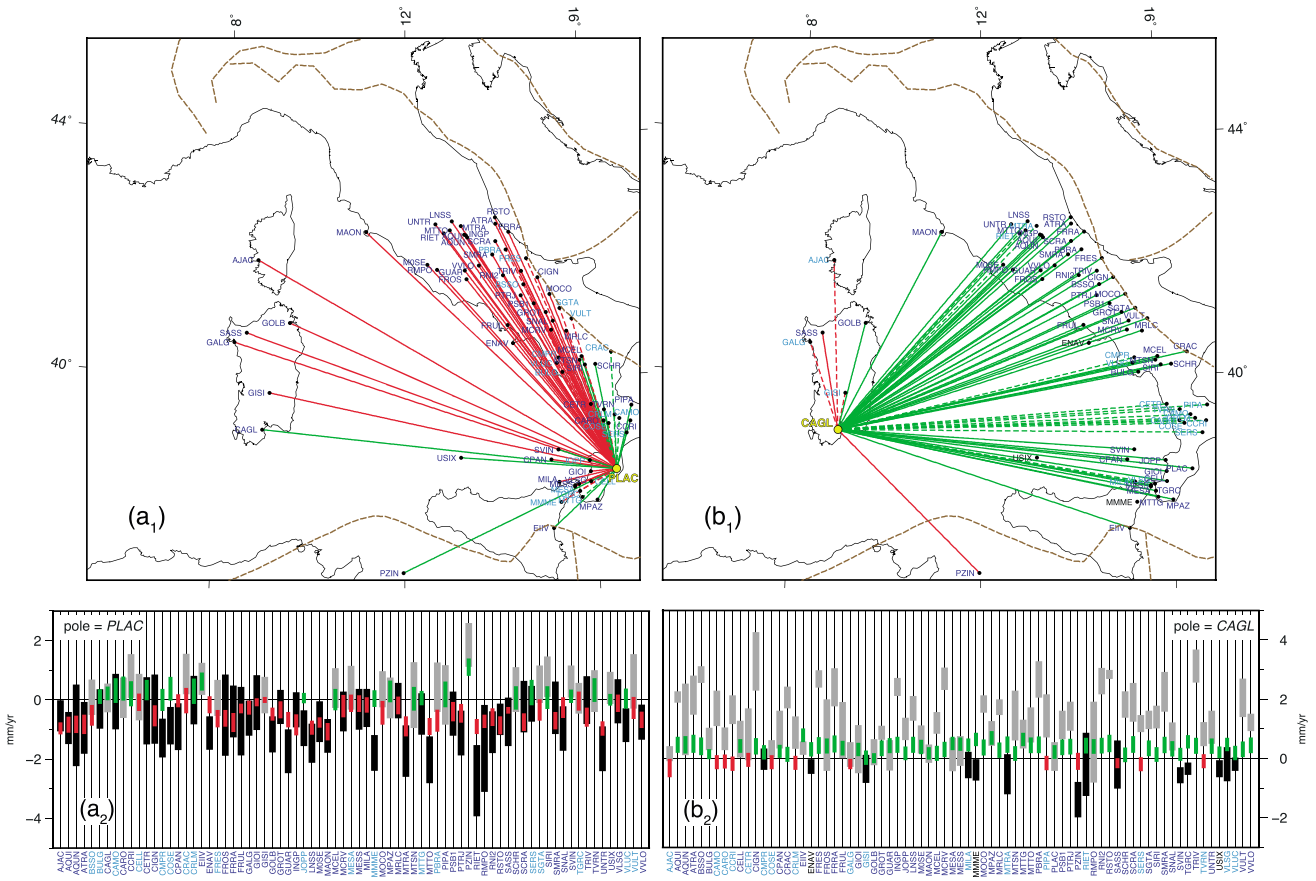

Figure 9. Local strain rate pattern that is predicted along the baselines that cross the south Tyrrhenian, which were computed with respect to poles (a_1) PLAC and (b_1) CAGL, for the best fit model gra_dia_per.25 (red lines indicate shortening; green lines indicate elongation). Continuum lines are used when a good agreement between the predicted and geodetic strain rates is obtained. Dashed lines are used when the predicted and geodetic strain rates exhibit opposite trends but reconcile within their uncertainties. In Figures $9a_2$ and $9b_2$, the predicted (red for shortening and green for elongation) and geodetic (filled black rectangles for shortening and gray rectangles for elongation) baseline rate values are compared with their uncertainties for poles (a_2) PLANC and (b_2) CAGL. The text is colored in blue when the predicted and geodetic baseline rate values agree, light blue is used when the predicted and geodetic baseline rate values reconcile within their uncertainties, and black is used when the agreement is poor.

The χ^2 of the Apulia domain (Figure 7f), which is close to the Calabrian Arc complex, became affected by variations in the boundary conditions, with gra_gra_per.0% being the best fit model. Furthermore, the higher values of χ^2 indicated that the agreement between the model and data in this domain worsened. This effect is foreseeable being the entire Adria domain considered to be kinematically independent from the Tyrrhenian domain [e.g., *D'Agostino et al*., 2011; *Serpelloni et al*., 2010; *Battaglia et al*., 2004].

The different best fit lithospheric stratifications in different areas of the study domain, including gra_dia_per in the south Tyrrhenian and gra_gra_per in the surrounding areas, reflect lateral heterogeneities in the lithospheric composition.

The best fit model gra_dia_per.25% in Figures $8a_1$ and $8b_1$ shows two examples of the large-scale strain pattern that is predicted along the baselines that cross the Tyrrhenian area. Although the model tends to underestimate the intensity of the regional strain rate (Figures $8a_2$ and $8b_2$), good agreement between the observed and predicted strain rates is obtained, with compression (red solid lines) characterizing the NW-SE baselines and extension (green solid lines) characterizing the SW-NE baselines. Dashed lines indicate baselines that reconcile within their uncertainties, although the predicted and observed strain rates exhibit opposite trends (Figures $8a_2$ and $8b_2$). Disagreement between the modeled and predicted strain pattern occurs only along the baselines that connect the poles to a few GPS stations (black text in Figure 8).

In the south Tyrrhenian, the agreement between the predicted and the observed baseline rates is better, and the deformation style and the intensity of the strain rate are also reproduced along several baselines (Figure 9).

7. Conclusions

This application of a novel statistical analysis strengthens the role of the Calabrian Arc complex in controlling the intraplate propagation of the tectonic stress that is related to the Africa-Eurasia convergence to the north.

In particular, a thermomechanical model was used to predict the strain rate along baselines that cross the area from the Calabrian Arc complex to the Alpine domain at both the regional and local scales. The predicted strain pattern was then compared to that derived from the GPS velocity solutions though a χ^2 test, in which both the data and model uncertainties were taken into account.

The implementation of a preliminary outlier detection scheme based on PCA enabled the identification and exclusion of GPS stations that may not be representative of the main tectonic process of interest from the comparative χ^2 test.

Our results suggest that the study area must be paved by a heterogeneous lithosphere that is characterized by a granite-type upper crust, diabase-type lower crust, and peridotite-type lithosphere mantle in the south Tyrrhenian and a granite-type upper crust, granulite-type lower crust, and peridotite-type lithosphere mantle in the surrounding area to reproduce the regionally observed SE-NW compression and SW-NE extension.

Furthermore, our results indicate that an important portion of the Africa-Eurasia convergence is not transmitted through the Calabrian Arc to high latitudes. In particular, at least 75% of the convergence is either absorbed by subduction or accommodated within the microblocks when the strain pattern is analyzed at the local scale in the surroundings of the Calabrian Arc.

In both cases, our results confirm that the Africa-Eurasia tectonics affect the deformation to the northern border of the Alps and beyond [*Marotta and Sabadini*, 2004]. However, small variations in tectonic forcing along the limited border of the Calabrian Arc can affect the deformation in the south Tyrrhenian.

Appendix A: Mathematical Formulation of the Problem and Values of the Parameters That Were Used in the Analysis

A1. Mathematical Formulation of the Problem

Vertically integrated momentum equations

$$\frac{1}{\sin\widehat{\phi}}\frac{\partial}{\partial\vartheta}\left[\overline{\mu}\left(\frac{1}{\sin\widehat{\phi}}\frac{\partial u_{\vartheta}}{\partial\vartheta}-\frac{\partial u_{\widehat{\phi}}}{\partial\widehat{\phi}}+u_{\widehat{\phi}}\cot\widehat{\phi}\right)\right]+\frac{\partial}{\partial\widehat{\phi}}\left[\overline{\mu}\left(\frac{1}{\sin\widehat{\phi}}\frac{\partial u_{\widehat{\phi}}}{\partial\vartheta}+\frac{\partial u_{\vartheta}}{\partial\widehat{\phi}}-u_{\vartheta}\cot\widehat{\phi}\right)\right]$$
$$+\left[2\overline{\mu}\left(\frac{1}{\sin\widehat{\phi}}\frac{\partial u_{\widehat{\phi}}}{\partial\vartheta}+\frac{\partial u_{\vartheta}}{\partial\widehat{\phi}}-u_{\vartheta}\cot\widehat{\phi}\right)\right]\cot\widehat{\phi}=\frac{1}{\sin\widehat{\phi}}\frac{\partial}{\partial\vartheta}\left[\frac{g\rho_m R}{2H_L}\left(1-\frac{\rho_c}{\rho_m}\right)S^2\right]$$

$$\frac{1}{\sin\widehat{\phi}}\frac{\partial}{\partial\vartheta}\left[\overline{\mu}\left(\frac{1}{\sin\widehat{\phi}}\frac{\partial u_{\widehat{\phi}}}{\partial\vartheta}+\frac{\partial u_{\vartheta}}{\partial\widehat{\phi}}-u_{\vartheta}\cot\widehat{\phi}\right)\right]-\frac{\partial}{\partial\widehat{\phi}}\left[\overline{\mu}\left(\frac{1}{\sin\widehat{\phi}}\frac{\partial u_{\vartheta}}{\partial\vartheta}-\frac{\partial u_{\widehat{\phi}}}{\partial\widehat{\phi}}+u_{\widehat{\phi}}\cot\widehat{\phi}\right)\right]$$
$$-\left[2\overline{\mu}\left(\frac{1}{\sin\widehat{\phi}}\frac{\partial u_{\vartheta}}{\partial\vartheta}-\frac{\partial u_{\widehat{\phi}}}{\partial\widehat{\phi}}+u_{\widehat{\phi}}\cot\widehat{\phi}\right)\right]\cot\widehat{\phi}=\frac{\partial}{\partial\widehat{\phi}}\left[\frac{g\rho_m R}{2H_L}\left(1-\frac{\rho_c}{\rho_m}\right)S^2\right]$$

Energy equation

$$\nabla\cdot(K\nabla T)+\rho H=0$$

u_{ϑ} and $u_{\widehat{\phi}}$ are the velocity components along the longitude ϑ and the colatitude $\widehat{\phi}$, respectively; S is the crustal thickness; H_L is the lithosphere thickness; ρ_c and ρ_m are the densities of the crust and mantle; K is the thermal conductivity; T is the temperature; and H radiogenic heat production.

$\overline{\mu}=(1/\dot{\varepsilon})\int_0^{H_L}\sigma_y dy$ Effective viscosity,

$\sigma_{\text{Brittle}}=\beta\, r\rho\, g;\ \beta=3$ (thrust) 1.2 (strike slip) 0.75 (normal)

$\sigma_y=\min\{\sigma_{\text{Brittle}},\sigma_{\text{Ductile}}\}$ Lithosphere strength

$\sigma_{\text{Ductile}}=\left(\frac{\dot{\varepsilon}}{\dot{\varepsilon}_o}\right)^{\frac{1}{n}}\cdot\exp\left(\frac{E_a}{nRT}\right);\ \dot{\varepsilon}=10^{-19}\div10^{-16}\ \text{s}^{-1}$

Table A1. Lithological Stratification

Model Name	Upper Crust	Lower Crust	Mantle
gra_gra_per	Granite	Granulite	Peridotite
gra_dia_per	Granite	Diabase	Peridotite
qtz_dia_oli	Quartzite	Diabase	Olivine

Table A2. Values of the Parameters Used in the Analysis

Name	Granite	Quartzite	Granulite	Diabase	Peridotite	Olivine
Density ρ (kg/m^3)	$2650 \div 2750^a$	$2650 \div 2750^a$	$2800 \div 2900^a$	$2850 \div 2900^{f,g}$	$3200 \div 3300^a$	$3200 \div 3300^a$
Radiogenic Heat Production H (10^{-6} W m^{-3})	$1.74 \div 3.23^a$	$1.74 \div 3.23^a$	$0.15 \div 0.5^a$	$0.179 \div 0.722^a$	$0.002 \div 0.03^a$	$0.002 \div 0.03^a$
Conductivity K (W m^{-1} K^{-1})	$2.5 \div 3.0^b$	$2.5 \div 3.0^b$	$2.0 \div 2.5^b$	$2.0 \div 4.0^c$	$3.0 \div 4.15^{b,d}$	$3.0 \div 4.15^{b,d}$
Activation Energy E_a (10^3 J mol^{-1})	$123 \div 137^e$	$154 \div 156^e$	$243 \div 485^f$	$260 \div 485^f$	$471 \div 532^h$	$498 \div 535^g$
$\dot{\varepsilon}_o$ (Pa^{-n} s^{-1})	$7.94328 \times 10^{-16} \div 79.245 \times 10^{-30e}$	$3.99052 \times 10^{-18} \div 2.51189 \times 10^{-24e}$	$20.095 \times 10^{-22} \div 8.8334 \times 10^{-22f}$	$7.96214 \times 10^{-25} \div 5.04766 \times 10^{-28f}$	$2.0 \times 10^{-21} \div 2.5 \times 10^{-17h}$	$5.49713 \times 10^{-25} \div 4.85 \times 10^{-17g}$
n	$1.9 \div 3.2^e$	$2.3 \div 2.4^e$	$3.1 \div 4.2^f$	$3.4 \div 4.7^f$	$3.5 \div 4.0^h$	$3.5 \div 4.48^g$

[a] *Vilà et al.* [2010].
[b] *Artemieva and Mooney* [2001].
[c] *Turcotte and Schubert* [2002].
[d] *Rybach* [1988].
[e] *Ranalli and Murphy* [1987].
[f] *Afonso and Ranalli* [2004].
[g] *Burov* [2010].
[h] *Chopra and Peterson* [1981].

Acknowledgments
This work was supported by the SISMA project, ASI contract I/093/06/0. No new data were used in producing this paper. All the used data are properly cited and referred to in the reference list. All the figures were created using GMT plotting software [*Wessel and Smith*, 2001]. The Editors and the two reviewers are thanked for the constructive criticisms and suggestions.

References

Afonso, J. C., and G. Ranalli (2004), Crustal and mantle strength in continental lithosphere: Is the jelly sandwich model obsolete?, *Tectonophysiscs*, *394*, 221–232.
Altamini, Z., X. Collieliux, J. Legagrand, B. Garayt, and C. Boucher (2007), ITRF2005: A new release of the International Terrestrial Reference Frame based on time series of station positions and Earth Orientation Parameters, *J. Geophys. Res.*, *112*, B09401, doi:10.1029/2007JB004949.
Argnani, A. (2009), Evolution of the southern Tyrrhenian slab tear and active tectonics along the western edge of the Tyrrhenian subducted slab, in *Collision and Collapse at the Africa-Arabia-Eurasia Subduction Zone*, edited by D. J. J. Van Hinsbergen, M. A. Edwards, and R. Govers, *Geol. Soc. Spec. Publ.*, *311*, 193–212, doi:10.1144/SP311.7.
Artemieva, I., and W. D. Mooney (2001), Thermal thickness and evolution of Precambrian lithosphere: A global study, *J. Geophys. Res.*, *106*(B8), 16,387–16,414, doi:10.1029/2000JB900439.
Barba, S., M. M. C. Carafa, M. T. Mariucci, P. Montonr, and S. Pierdominici (2010), Present-day stress-field modeling of southern Italy constrained by stress and GPS data, *Tectonophysics*, *482*, 193–204, doi:10.1016/j.tecto.2009.10.017.
Barzaghi, R., A. M. Marotta, R. Splendore, C. De Gaetani, and A. Borghi (2014), Statistical assessment of a predictive modeling uncertainty: A geophysical case study, *Geophys. J. Int.*, *197*(1), 22–32, doi:10.1093/gji/ggt510.
Bassi, G., R. Sabadini, and S. Rebaï (1997), Modern tectonic regime in the Tyrrhenian area: Observations and models, *Geophys. J. Int.*, *129*, 330–346.
Battaglia, M., M. H. Murray, E. Serpelloni, and R. Burgmann (2004), The Adriatic region: An independent microplate within the Africa-Eurasia collision zone, *Geophys. Res. Lett.*, *31*, L09605, doi:10.1029/2004GL019723.
Burov, E. R. (2010), The equivalent elastic thickness (Te), seismicity and long-term rheology of continental lithosphere: Time to burn-out cream-brulëe? Insights from large-scale geodynamic modeling, *Tectonophysics*, *484*, 4–26.
Chiarabba, C., P. De Gregori, and F. Speranza (2008), The southern Tyrrhenian subduction zone: Deep geometry, magmatism and Plio-Pleistocene evolution, *Earth Planet. Sci. Lett.*, *268*, 408–423.
Chopra, P. N., and M. S. Peterson (1981), The experimental deformation of dunite, *Tectonophysics*, *78*, 453–473.
D'Agostino, N., and G. Selvaggi (2004), Crustal motion along the Eurasia-Nubia plate boundary in the Calabrian Arc and Sicily and active extension in the Messina Straits from GPS measurements, *J. Geophys. Res.*, *109*, B11402, doi:10.1029/2004JB002998.
D'Agostino, N., A. Avallone, D. Cheloni, E. D'Anastasio, S. Mantenuto, and G. Selvaggi (2008), Active tectonics of the Adriatic region from GPS and earthquake slip vectors, *J. Geophys. Res.*, *113*, B12413, doi:10.1029/2008JB005860.
D'Agostino, N., E. D'Anastasio, A. Gervasi, I. Guerra, M. R. Nedimović, L. Seeber, and M. Steckler (2011), Forearc extension and slow rollback of the Calabrian Arc from GPS measurements, *Geophys. Res. Lett.*, *38*, L17304, doi:10.1029/2011GL048270.
DeMets, C., R. G. Gordon, D. F. Argus, and S. Stein (1994), Effect of recent revisions to the geomagnetic reversals time scale on estimates of current plate motions, *Geophys. Res. Lett.*, *21*, 2191–2194, doi:10.1029/94GL02118.
Devoti, R., A. Esposito, G. Pietrantonio, A. R. Pisani, and F. Riguzzi (2011), Evidence of large scale deformation patterns from GPS data in the Italian subduction boundary, *Earth Planet. Sci. Lett.*, *311*, 230–241.
Faccenna, C., T. W. Becker, F. P. Lucente, L. Jolivet, and F. Rossetti (2001), History of subduction and back-arc extension in the Central Mediterranean, *Geophys. J. Int.*, *145*, 809–820.
Hollstein, C., H. G. Kahle, A. Geiger, S. Jenny, S. Goes, and D. Giardini (2003), New GPS constraints on the Africa-Eurasia plate boundary zone in southern Italy, *Geophys. Res. Lett.*, *30*(18), 1935, doi:10.1029/2003GL017554.

Jolliffe, I. T. (2010), *Principal Component Analysis*, *Ser. Stat*., 2nd ed., 487 pp., Springer, New York.
Koulakov, I., M. K. Kaban, M. Tesauro, and S. A. P. L. Cloetingh (2009), P- and S-velocity anomalies in the upper mantle beneath Europe from tomographic inversion of ISC data, *Geophys. J. Int.*, *179*, 345–366.
Malinverno, A., and W. B. F. Ryan (1986), Extension on the Tyrrhenian Sea and shortening in the Apennines as result of arc migration driven by sinking of the lithosphere, *Tectonics*, *5*, 227–245, doi:10.1029/TC005i002p00227.
Markou, M., and S. Singh (2003), Novelty detection: A review—Part 1: Statistical approaches, *Signal Process.*, *83*, 2481–2497, doi:10.1016/j.sigpro.2003.07.018.
Marotta, A. M., and R. Sabadini (2004), The signatures of tectonics and glacial isostatic adjustment revealed by the strain rate in Europe, *Geophys. J. Int.*, *157*, 865–870, doi:10.1111/j.1365-246X.2004.02275.x.
Marotta, A. M., and R. Sabadini (2008), Africa–Eurasia kinematics control of long-wavelength tectonic deformation in the Central Mediterranean, *Geophys. J. Int.*, *175*, 742–754.
Marotta, A. M., R. Splendore, and R. Barzaghi (2015), An application of model uncertainty statistical assessment: A case study of tectonic deformation in the Mediterranean, *J. Geodyn.*, *85*, 24–31.
Minelli, L., and C. Faccenna (2010), Evolution of the Calabrian accretionary wedge (central Mediterranean), *Tectonics*, *29*, TC4004, doi:10.1029/2009TC002562.
Montone, P., M. T. Mariucci, S. Pondrelli, and A. Amato (2004), An improved stress map for Italy and surroundings regions (central Mediterranean), *J. Geophys. Res.*, *109*, B10410, doi:10.1029/2003JB002703.
Neri, G., B. Orecchio, C. Totaro, G. Falcone, and D. Presti (2009), Subduction beneath southern Italy close the ending: Results from seismic tomography, *Seismol. Res. Lett.*, *80*, 63–70.
Neri, G., A. M. Marotta, B. Orecchio, D. Presti, C. Totaro, R. Barzaghi, and A. Borghi (2012), How lithospheric subduction changes along the Calabrian Arc in southern Italy: Geophysical evidences, *Int. J. Earth Sci. (Geol. Rundsch.)*, *101*, 1949–1969, doi:10.1007/s00531-012-0762-7.
Nocquet, J. M., E. Calais, A. Altamini, P. Sillard, and C. Boucher (2001), Intraplate deformation in western Europe deduced from an analysis of the International Terrestrial Reference Frame 1997 (ITRF97) velocity field, *J. Geophys. Res.*, *106*(B6), 11,239–11,257, doi:10.1029/2000JB900410.
Palano, M. (2015), On the present-day crustal stress, strain-rate fields and mantle anisotropy pattern of Italy, *Geophys. J. Int.*, *200*, 967–983, doi:10.1093/gji/ggu451.
Palano, M., L. Ferranti, C. Monaco, M. Mattia, M. Aloisi, V. Bruno, F. Cannavò, and G. Siligato (2012), GPS velocity and strain fields in Sicily and southern Calabria, Italy: Updated geodetic constraints on tectonic block interaction in the central Mediterranean, *J. Geophys. Res.*, *117*, B07401, doi:10.1029/2012JB009254.
Piromallo, C., and Morelli, A. (2003), *P* wave tomography of the mantle under the Alpine–Mediterranean area, *J. Geophys. Res.*, *108*(B2), 2065, doi:10.1029/2002JB001757.
Presti, D., A. Billi, B. Orecchio, C. Totaro, C. Faccenna, and G. Neri (2013), Earthquake focal mechanisms, seismogenic stress, and seismotectonics of the Calabrian Arc, Italy, *Tectonophysics*, *602*, 153–175, doi:10.1016/j.tecto.2013.01.030.
Ranalli, G., and D. C. Murphy (1987), Rheological stratification of the lithosphere, *Tectonophysics*, *132*, 281–295.
Rybach, L. (1988), Determination of heat production rate, in *Handbook of Terrestrial Heat Flow Density Determination*, edited by R. Haenel, L. Rybach, and L. Stegena, pp. 125–142, Kluwer Acad., Dordrecht, Netherlands.
Selvaggi, G., and C. Chiarabba (1995), Seismicity and P-velocity image of the southern Tyrrhenian subduction zone, *Geophys. J. Int.*, *121*, 818–826, doi:10.1111/j.1365-246X.1995.tb06441.x.
Serpelloni, E., R. Bürgmann, M. Anzidei, P. Baldi, B. Mastrolembo Ventura, and E. Boschi (2010), Strain accumulation across the Messina Straits and kinematics of Sicily and Calabria from GPS data and dislocation modeling, *Earth Planet. Sci. Lett.*, *298*, 347–360.
Splendore, R., A. M. Marotta, R. Barzaghi, A. Borghi, and L. Cannizzaro (2010), Block model versus thermomechanical model: New insights on the present-day regional deformation in the surroundings of the Calabrian Arc, in *Advances in Interpretation of Geological Processes: Refinement of Multiscale Data and Integration in Numerical Modelling*, edited by M. I. Spalla, A. M. Marotta, and G. Gosso, *Geol. Soc. London Spec. Publ.*, *332*, 129–147.
Turcotte, D. L., and G. Schubert (2002), *Geodynamics*, Cambridge Univ. Press, New York.
Vilà, M., M. Fernández, and I. Jiménez-Munt (2010), Radiogenic heat production variability of some common lithological groups and its significance to lithospheric thermal modeling, *Tectonophysics*, *490*, 152–264.
Wessel, P., and W. M. Smith (2001), New improved version of generic mapping tools released, *Eos Trans. AGU*, *79*, 579, doi:10.1029/98EO00426.
Wortel, M. J. R., and W. Spakman (2000), Subduction and slab detachment in the Mediterranean–Carpathian region, *Science*, *290*(5498), 1910–1917.